

# Multi-year composite view of ozone enhancements and stratosphere-to-troposphere transport in dry intrusions of northern hemisphere extratropical cyclones

Lyatt Jaeglé<sup>1</sup>, Robert Wood<sup>1</sup>, and Krzysztof Wargan<sup>2,3</sup>

<sup>1</sup>Department of Atmospheric Sciences, University of Washington, Seattle, Washington, USA

<sup>2</sup>Science Systems and Applications Inc., Lanham, Maryland, USA

<sup>3</sup>Global Modeling and Assimilation Office, NASA Goddard Space Flight Center, Greenbelt, Maryland, USA

Corresponding author: Lyatt Jaeglé ([jaegle@uw.edu](mailto:jaegle@uw.edu))

## Key Points:

- Satellite and reanalysis composites of extratropical cyclones display distinct ozone enhancements in the dry intrusion air stream
- These ozone enhancements maximize in spring, reaching values of 210 ppbv and 27 ppbv at 261 hPa and 464 hPa, respectively
- Dry intrusions lead to a flux of  $119 \text{ Tg O}_3 \text{ yr}^{-1}$ , or 42% of the northern hemisphere stratosphere-to-troposphere flux

*Accepted for publication in the Journal of Geophysical Research, Nov. 2017.*

**Abstract.** We examine the role of extratropical cyclones in stratosphere-to-troposphere (STT) exchange with cyclone-centric composites of  $\text{O}_3$  retrievals from the Microwave Limb Sounder (MLS) and the Tropospheric Emission Spectrometer (TES), contrasting them to composites obtained with the Modern-Era Retrospective-analysis for Research and Applications (MERRA and MERRA-2) reanalyses and the GEOS-Chem chemical transport model. We identify 15,978 extratropical cyclones in the northern hemisphere (NH) for 2005-2012. The lowermost stratosphere (261 hPa) and middle troposphere (424 hPa) composites feature a 1,000 km-wide  $\text{O}_3$  enhancement in the dry intrusion (DI) airstream to the southwest of the cyclone center, coinciding with a lowered tropopause, enhanced potential vorticity, and decreased  $\text{H}_2\text{O}$ . MLS composites at 261 hPa show that the DI  $\text{O}_3$  enhancements reach a 210 ppbv maximum in April. At 424 hPa, TES composites display maximum  $\text{O}_3$  enhancements of 27 ppbv in May. The magnitude and seasonality of these enhancements are captured by MERRA and MERRA-2, but GEOS-Chem is a factor of two too low. The MERRA-2 composites show that the  $\text{O}_3$ -rich DI forms a vertically aligned structure between 300 and 800 hPa, wrapping cyclonically with the warm conveyor belt. In winter and spring DIs,  $\text{O}_3$  is enhanced by 100 ppbv or 100-130% at 300 hPa, with significant enhancements below 500 hPa (6-20 ppbv or 15-30%). We estimate that extratropical cyclones result in a STT flux of  $119 \pm 56 \text{ Tg O}_3 \text{ yr}^{-1}$ , accounting for  $42 \pm 20 \%$  of the NH extratropical  $\text{O}_3$  STT flux. The STT flux in cyclones displays a strong dependence on westerly 300 hPa wind speeds.

# 1 Introduction

Constraining the contribution of stratosphere-troposphere exchange (STE) to the tropospheric O<sub>3</sub> budget has been a long-standing issue [Monks *et al.*, 2000; Meloen *et al.*, 2003; Stohl *et al.*, 2003]. Despite decades of research on this topic, the current generation of chemical transport models show large discrepancies in their STE fluxes of O<sub>3</sub>, which affects their predicted concentrations of tropospheric O<sub>3</sub> and the relative contribution from photochemical production [Stevenson *et al.*, 2006; Wu *et al.*, 2007; Wild *et al.*, 2007; Young *et al.*, 2013]. Furthermore, a significant fraction of tropospheric O<sub>3</sub> variability is linked to variability and trends in STE, which can be difficult to untangle from trends in O<sub>3</sub> production due to changing precursor emissions [e.g., Fusco and Logan, 2003; Jaffe *et al.*, 2003; Hsu and Prather, 2009; Langford *et al.*, 2009; Logan *et al.*, 2012; Parrish *et al.*, 2012; Hess and Zbinden, 2013; Neu *et al.*, 2014; Cooper *et al.*, 2012; Lin *et al.*, 2012; Strode *et al.*, 2013; Verstraeten *et al.*, 2015]. O<sub>3</sub> is a central player in the oxidizing capacity of the troposphere, an effective greenhouse gas in the upper troposphere and a key pollutant in surface air. This persistent uncertainty in O<sub>3</sub> STE thus erodes our confidence in model estimates of how stratospheric O<sub>3</sub> influences air quality and climate.

On a global scale, STE is driven by the propagation of Rossby waves into the stratosphere and mesosphere, which lead to slow ascent from the troposphere to the stratosphere in the tropics, quasi-isentropic transport between the tropical stratosphere and extratropical stratosphere, and downward flow at mid- and high-latitudes [e.g., Holton *et al.*, 1995]. However, observations show that in the extratropics, instead of a continuous downward flow, STE occurs episodically in association with mesoscale and synoptic-scale processes [Stohl *et al.*, 2003], including perturbations of the tropopause due to extratropical cyclones [e.g., Reed and Sanders, 1953; Danielsen, 1968; Lamarque and Hess, 1994; Holton *et al.*, 1995; Rood *et al.*, 1997; Wirth and Egger, 1999; Wernli and Bourqui, 2002]. For example, in every extratropical cyclone that they sampled over the U.S., Johnson and Viezee [1981] found stratospheric O<sub>3</sub> intrusions extending down to ~3-5 km altitude. They proposed that all low-pressure systems at midlatitudes may be accompanied by transport of stratospheric air into the troposphere, to a degree proportional to the intensity of the storm. Since these early observations, numerous other studies have demonstrated transport of stratospheric air with high O<sub>3</sub> within the tropopause folds (i.e. a region of locally lowered tropopause or with multiple tropopauses) and cut-off cyclones associated with extratropical cyclones [e.g. Danielsen, 1980; Moody *et al.*, 1996; Beekman *et al.*, 1997; Cooper *et al.*, 1998, 2004; Sullivan *et al.*, 2015; Škerlak *et al.*, 2015; Ott *et al.*, 2016].

Transport within extratropical cyclones typically follows the warm conveyor belt (WCB) and dry intrusion (DI) airstreams. The WCB originates at low levels in the warm sector of the cyclone and travels poleward, rapidly ascending to the mid- and upper troposphere [e.g., Browning and Roberts, 1994]. As this warm moist air rises along moist isentropes, it leads to intense precipitation and the formation of the typical comma shaped cloud associated with mature cyclones [Carlson, 1980] as illustrated in Figure 1. The O<sub>3</sub>-rich DI (also referred to as dry airstream, DA) starts in the upper troposphere/lower stratosphere (UT/LS) to the west of the cyclone center near the tropopause fold, and then fans out as it descends towards low levels behind the cold front [Browning, 1997]. The cold dry air of the DI leads to the formation of the ‘dry slot’ providing a sharp westward limit to most of the clouds and precipitation (Figure 1). The WCB and DI can each split into two branches (labelled A-D in Figure 1), depending on upper level circulation [e.g., Thorncroft *et al.*, 1993]. These branches form two distinct

1 baroclinic life cycles (LC), which can be either anticyclonic (LC1, formed by branches A and D)  
2 resulting in elongated streamers [Appenzeller and Davies, 1992] or cyclonic (LC2, branches B  
3 and C) forming a vortex vertically aligned with the surface low-pressure system [Whitaker et al.,  
4 1988].

5 Numerical modeling studies have provided estimates of the STE associated with  
6 extratropical cyclones based on individual case studies [e.g., Lamarque and Hess, 1994; Spaete  
7 et al., 1994; Wernli and Davies, 1997; Wirth and Egger, 1999; Olsen and Stanford, 2001],  
8 idealized cyclones [e.g., Bush and Peltier, 1994; Polvani and Esler, 2007] or more  
9 comprehensive regional studies [e.g., Reutter et al. 2015]. These studies highlight the large case-  
10 to-case variability of both the magnitude of the STE flux within each extratropical cyclone and  
11 the dominant mechanism responsible for irreversible mixing within the troposphere: turbulent  
12 mixing near the jet stream [Shapiro, 1980], stratospheric streamer fragmentation and roll-up  
13 [Appenzeller et al., 1996], localized wet convection [Langford and Reid, 1998], and breaking  
14 gravity waves [Cho et al., 1999; Pavelin and Whiteway, 2002].

15 In this paper, our goal is to examine more systematically the influence of extratropical  
16 cyclones on tropospheric O<sub>3</sub> concentrations and the associated stratosphere-to-troposphere (STT)  
17 O<sub>3</sub> flux. While the hemispheric-scale magnitude of the O<sub>3</sub> STE flux is controlled by the wave-  
18 driven Brewer-Dobson circulation, extratropical cyclones are one of the important tropopause  
19 gateways for this transport thereby determining the timing, location and depth of stratospheric O<sub>3</sub>  
20 intrusions within the troposphere.

21 We use a cyclone-centric compositing approach to examine O<sub>3</sub> enhancements in the DIs  
22 of northern hemisphere (NH) extratropical cyclones as observed by the Microwave Limb  
23 Sounder (MLS) and Tropospheric Emissions Spectrometer (TES) over an 8-year period (2005-  
24 2012). The short spatiotemporal scales of STE transport (~ hours-days, 100s-1000s km  
25 horizontally and 100s-1000s m vertically) represent a fundamental difficulty for their  
26 observations with the small swaths of MLS and TES. Because of this, only a few individual  
27 stratospheric intrusions have been studied with these instruments [e.g., Manney et al., 2009;  
28 2011; Tang and Prather, 2012]. We will demonstrate that compositing a large number of  
29 extratropical cyclones is a powerful approach to overcome this limitation. Our results will show  
30 that robust chemical patterns emerge from these space-based observations composites of  
31 extratropical cyclones. We will assess the ability of two reanalyses (Modern-Era Retrospective  
32 Analysis for Research and Applications: MERRA and MERRA-2) and a chemical transport  
33 model (GEOS-Chem) in reproducing these patterns.

34 In Section 2 we describe the satellite observations and models used in this work. Our  
35 cyclone identification and compositing methodology is outlined in Section 3. We then present O<sub>3</sub>  
36 composites of satellite observations, reanalyses, and GEOS-Chem in the lower stratosphere at  
37 261 hPa and middle troposphere at 464 hPa (Section 4). In Section 5, we use MERRA-2  
38 reanalysis composites to examine the three-dimensional structure of stratospheric O<sub>3</sub> intrusions  
39 within extratropical cyclones and how this structure varies with season. Finally, in Section 6 we  
40 quantify the contribution of these intrusions to O<sub>3</sub> STT flux before summarizing our results  
41 (Section 7).

## 2 Satellite observations, reanalysis and model data sets used in this analysis

### 2.1 Satellite observations

We use O<sub>3</sub> retrievals from the Microwave Limb Sounder (MLS) instrument [Waters *et al.*, 2006] onboard NASA's Aura satellite launched on 15 July 2004, on a sun-synchronous polar orbit at 705 km altitude. MLS is a limb scanning instrument retrieving O<sub>3</sub> vertical profiles from the 240 GHz radiances, with a horizontal resolution of 6-km cross-track and 200 km along-track, and 38 pressure levels between 261 hPa and 0.02 hPa. We use MLS Level 2 v4.2 O<sub>3</sub> retrievals for 2005-2012 at 261 hPa to which we apply the data screening recommended by Livesey *et al.* [2017]. MLS can retrieve O<sub>3</sub> in moderately cloudy conditions, but scattering from thick clouds can adversely influence the retrievals and the affected profiles are removed with the data screening. Wargan *et al.* [2015] found that MLS v3.3 O<sub>3</sub> at 261 hPa (which is very similar to MLS v4.2 O<sub>3</sub> at midlatitudes) displayed a systematic 60 ppbv positive bias compared to ozonesonde observations at northern midlatitudes. To take this bias into account we subtract 60 ppbv from the MLS O<sub>3</sub> retrievals.

The Aura satellite Tropospheric Emission Spectrometer (TES) instrument [Beer *et al.*, 2006], has a footprint of 8 km by 5 km and measures upwelling radiances in the infrared. Tropospheric TES O<sub>3</sub> retrievals have 1-2 degrees of freedom for signal (1-2 independent pieces of information on the vertical distribution of O<sub>3</sub>). We use data from the TES L2 "lite" product, version 6 for 2005-2012 at the 464 hPa level, which is broadly representative of the free troposphere. We screen the data for good quality, excluding scenes with large optical depth clouds and O<sub>3</sub> c-curve [Herman and Kulawik, 2013]. In a validation with coinciding ozonesonde measurements for 2005-2010, Verstraeten *et al.* [2013] report a TES positive bias of +7 ppbv (+13%) at northern midlatitudes. Following their recommendation we correct the TES O<sub>3</sub> retrievals with season-dependent regression coefficients (Table 3 in Verstraeten *et al.*, 2013).

The Atmospheric Infrared Sounder (AIRS) onboard the NASA Aqua satellite has been operating since 2002 [Auman *et al.*, 2003]. AIRS observes the Earth in the infrared between 3.7 and 15.4  $\mu\text{m}$ , with a footprint size of  $\sim 13.5$  km, and vertical resolution of  $\sim 2$  km. We use daily AIRS level 3 V6 H<sub>2</sub>O retrievals at 300 hPa for 2005-2012, at a resolution of  $1^\circ \times 1^\circ$ . Validation of AIRS specific humidity against aircraft, balloons, and radiosondes generally show agreement to within 15-25% in the free troposphere [e.g., Tian *et al.*, 2013 and references therein].

### 2.2 Reanalysis and model data sets

The Modern-Era Retrospective Analysis for Research and Applications (MERRA; Rienecker *et al.*, 2011) reanalysis consists of the GEOS-5 atmospheric general circulation model (AGCM) and a 3DVAR analysis algorithm based on the Gridpoint Statistical Interpolation (GSI) scheme with a 6-hour update cycle. MERRA has a grid of  $0.5^\circ$  latitude  $\times$   $2/3^\circ$  longitude with 72 vertical levels from the surface to 0.01 hPa, with a  $\sim 1$  km vertical resolution in the UT/LS. MERRA assimilates O<sub>3</sub> profiles from a series of NOAA Solar Backscatter Ultraviolet (SBUV/2) instruments [Frederick *et al.*, 1986; Bhartia *et al.*, 2004]. The AGCM transports the assimilated O<sub>3</sub> using the assimilated meteorology, with a parameterized representation of chemistry based on monthly zonally symmetric O<sub>3</sub> production rates and loss frequencies derived from the Goddard two-dimensional chemistry and transport model [Douglass *et al.*, 1996] using the procedure

described in *Stajner et al.* [2008]. We use daily averaged 3-hourly MERRA reanalysis O<sub>3</sub> fields on a 1.25° × 1.25° resolution grid.

The Modern-Era Retrospective Analysis for Research and Applications, Version 2 (MERRA-2, *Gelaro et al.*, 2017) is the latest NASA reanalysis, with significant changes to the AGCM [*Molod et al.*, 2015] and the observing system [*McCarty et al.*, 2016], compared to MERRA. One of the improvements is the assimilation of Aura's Ozone Monitoring Instrument (OMI) v8.5 total column O<sub>3</sub> data and MLS O<sub>3</sub> profiles, starting in October 2004, as described in *Wargan et al.* [2017]. For the 2005-2012 period of our analysis, MERRA-2 assimilates MLS v2.2 O<sub>3</sub> profiles from 215 hPa to 0.02 hPa on 21 levels. While 261 hPa MLS data was not used in MERRA-2 for this period, this level still contains information from the assimilation of MLS observations at higher levels and from OMI constraining the total column, which are then redistributed according to the analysis dynamics. The same 2D monthly O<sub>3</sub> production rates and loss frequencies are used as in MERRA. We use MERRA-2 reanalysis 3-hourly O<sub>3</sub> fields (daily averaged) at a 0.5° latitude × 0.635° longitude resolution and the same vertical resolution as MERRA. The MERRA-2 constituent, dynamical, cloud and precipitation fields used in this study are taken from the assimilated product [*GMAO* 2015a-f].

Both MERRA and MERRA-2 show a good representation of stratospheric vertical O<sub>3</sub> profiles observed by SAGE II, with a bias of less than 5% in the extratropics [*Wargan et al.*, 2017]. Once OMI and MLS O<sub>3</sub> observations are assimilated in MERRA-2 (starting in late 2004), the MERRA-2 bias decreases to less than 2%, with an improved representation of the observed variability and of the sharp O<sub>3</sub> gradient across the tropopause. *Wargan et al.* [2017] find that MERRA-2 displays very good agreement with ozonesonde observations in the stratosphere, where the bias is generally less than 5% (1.2% between 30°N and 60°N with 0.98 correlation). In the upper troposphere, they report that MERRA-2 is biased low by 13.6% (correlation of 0.9) compared to ozonesondes at 30-60°N. MERRA displays a smaller bias (<10%). They attribute this MERRA-2 low UT bias to the low sensitivity of OMI columns to O<sub>3</sub> below 500 hPa and the lack of detailed tropospheric NO<sub>x</sub> chemistry in the assimilation system [*Wargan et al.*, 2015]. The recent work of *Knowland et al.* [2017] shows that MERRA-2 captures the vertical structure and timing of stratospheric intrusions reaching the surface in a case study over the western United States.

We conduct a 2005-2012 tagged O<sub>3</sub> simulation with the GEOS-Chem chemical transport model [*Bey et al.*, 2001] driven by MERRA meteorological fields temporally averaged over 3 hours (1 hour for surface variables). The MERRA fields are degraded from their horizontal native resolution to 2°×2.5°. The tagged O<sub>3</sub> simulation [*Wang et al.*, 1998; *Liu et al.*, 2002] uses archived daily three-dimensional tropospheric O<sub>3</sub> production and loss frequencies calculated with the GEOS-Chem full chemistry simulation. Stratospheric O<sub>3</sub> concentrations are calculated with the Linoz linearized chemical scheme [*McLinden et al.*, 2000]. The GEOS-Chem tagged O<sub>3</sub> simulation (v9-01-03) includes two tracers: total O<sub>3</sub> and O<sub>3</sub> produced in the stratosphere. The global STE flux calculated with GEOS-Chem is 450±30 Tg O<sub>3</sub> yr<sup>-1</sup> for the 2005-2012 period.

### 3 Methodology

Cyclone-relative compositing has been successfully used to examine many meteorological aspects of cyclones and their regional characteristics [e.g., *Manobianco*, 1989;

1 *Lau and Crane, 1995; Chang and Song, 2006; Field and Wood, 2007; Dacre and Gray, 2009;*  
2 *Naud et al., 2012; Grandey et al., 2013*]. While compositing hides case-to-case variability, the  
3 main advantage of this technique is that it provides a more general view of extratropical cyclones  
4 than individual case studies do, allowing to extract common patterns. In addition, composites  
5 allow for a useful framework to test whether climate and weather models simulate realistic  
6 cyclones in terms of their structure, precipitation, clouds, and wind fields [e.g., *Klein and Jakob,*  
7 *1999; Field et al., 2008; Catto et al., 2010; Govekar et al., 2013; Naud et al., 2014*].

8 Here, we follow a three-step approach consisting of a) identifying extratropical cyclones  
9 based on sea level pressure, b) extracting daily satellite observations and reanalysis/model fields  
10 on a 4,000 km × 4,000 km grid centered on the cyclone center, and c) generating cyclone-centric  
11 composites as well as anomalies with respect to background conditions.

### 12 3.1 Identification of NH extratropical cyclones

13 We have adapted the method described in *Patoux et al. [2009]* to systematically identify  
14 NH extratropical cyclones using daily-averaged MERRA sea level pressure (SLP) fields. We  
15 identify a cyclone center if it fulfills the following criteria: (1) there is a true local pressure  
16 minimum (i.e., the surface pressure is less than at the 8 surrounding grid points); (2) the surface  
17 pressure is at least 1 hPa less than the pressure averaged over the surrounding grid points up to  
18 ±4 grid indices; (3) the Laplacian of pressure averaged over those same points is at least  $0.5 \times 10^{-10}$   
19  $\text{hPa m}^{-2}$ . When two or more cyclones occur within a 2000 km radius, we select the cyclone  
20 with the lowest SLP and eliminate the weaker cyclones from our database. We only consider  
21 cyclones with a central SLP lower than 1010 hPa and with 300 hPa potential vorticity (PV)  
22 greater than 1 pvu (PV units,  $1 \text{ pvu} = 10^{-6} \text{ m}^2 \text{ s}^{-1} \text{ K kg}^{-1}$ ). The SLP limit eliminates 12% of the  
23 cyclones identified, while the PV criterion eliminates another 21%. The PV threshold removes  
24 cyclones with little upper tropospheric signal and thus non-existent or weak dry intrusions. We  
25 note that with our simple approach we only identify the daily location of cyclones and do not  
26 track the evolution of their position over time.

27 For the period 2005-2012, we identify 15,978 extratropical cyclones with centers located  
28 poleward of 30°N. These cyclones are evenly spread by season, with slightly more cyclones  
29 detected during spring: 25% in winter (DJF), 28% spring (MAM), 22% in summer (JJA) and  
30 25% in fall (SON). Figure 2a shows our resulting annual mean cyclone frequency, which  
31 corresponds to the percentage of time that a given point is located within an extratropical  
32 cyclone. To generate this frequency, we obtain the size of individual cyclones from the  
33 maximum local SLP gradient following *Patoux et al. [2009]*. Geographically, most extratropical  
34 cyclones occur in the North Atlantic and North Pacific storm tracks (Figure 2a), as shown in  
35 many past studies on this topic [e.g., *Hoskins and Hodges, 2002; Wernli and Schwierz, 2006;*  
36 *Ulbrich et al., 2009*]. In the storm tracks, our cyclone frequency is 10-30% lower compared to  
37 these studies, as we do not consider cyclones with a weak central SLP and/or with little upper  
38 tropospheric signal.

### 39 3.2 Compositing approach

40 To generate cyclone-centric composites, we first interpolate all the datasets to the same  
41 global  $1^\circ \times 1^\circ$  grid. For each extratropical cyclone we translate and regrid the daily averaged

satellite, reanalysis and modeling products onto a 4,000 km  $\times$  4,000 km region centered over the cyclone center, following *Field and Wood* [2007]. The cyclone-centric grid has a 100-km horizontal grid spacing. All the cyclones are averaged together to generate annual and seasonal composites.

To examine the anomalies relative to background, for each cyclone and dataset we generate a separate cyclone-centric grid at the same location and date of the original cyclone but using instead a 60-day running mean of the 1° $\times$ 1° fields smoothed with a 6° wide boxcar average. We define the anomalies (e.g.,  $\Delta O_3$ ) as the difference between the composites of the cyclones and their background ( $\Delta O_3 = O_{3\text{cyclone}} - O_{3\text{background}}$ , in ppbv) or the enhancement relative to background ( $\Delta O_3 = 100 \times (O_{3\text{cyclone}} - O_{3\text{background}}) / O_{3\text{background}}$ , in %).

Figure 3 shows the annual mean 2005-2012 composites of several MERRA-2 meteorological parameters: precipitation, cloud fraction, windspeed at 300 hPa, tropopause height, PV at 300 hPa, and H<sub>2</sub>O at 300 hPa. We use the traditional dynamical tropopause definition, as the surface with a constant PV value of 2 pvu or the surface with a potential temperature of 380 K, whichever is lower [*Hoskins et al.*, 1985; *Holton et al.*, 1995]. Maximum precipitation occurs at the center of the composite, curving to the southeast with the characteristic comma shape [e.g., *Field and Wood*, 2007; *Naud et al.*, 2012]. High 300 hPa westerly wind speeds are seen to the southwest of the cyclone center, peaking at 35 m s<sup>-1</sup> in the jet stream (Figure 3c). The 500 hPa geopotential height (white contours in Figure 3d) form a distinct cut-off low near the cyclone center. The tropopause fold associated with the DI stands out in Figure 3d, with composite tropopause pressure reaching 360 hPa to the west of the cyclone center. This represents a 60 hPa increase in tropopause pressure relative to background conditions and is accompanied by a PV increase of 1-2 pvu and a 40-80 ppmv H<sub>2</sub>O decrease in the DI (Figure 3). The MERRA-2 H<sub>2</sub>O at 300 hPa is 40% larger than AIRS H<sub>2</sub>O (Figure 3fg), but the H<sub>2</sub>O anomalies relative to background conditions display the same pattern. We find a similar wet bias in MERRA relative to AIRS (not shown). A wet bias for MERRA and MERRA-2 was also noted by *Jiang et al.* [2015] in their comparison to MLS H<sub>2</sub>O in the UT/LS. *Tian et al.* [2013] suggested that part of the difference between MERRA and AIRS might be due to low sampling of AIRS in cloudy regions, particularly in the midlatitude storm tracks. Indeed, most of the cyclone composite has cloud fractions exceeding 50% (Figure 3b).

For each individual cyclone, we identify the DI at 300 hPa as the outermost closed PV contour enclosing a PV maximum within 1000 km of the cyclone center. Then, within this region, we extract the maximum tropopause pressure (lowest tropopause altitude), which we will use as an indicator of the lowest altitude reached by the DI. Figure 2b shows a two-dimensional histogram of the number of cyclones as a function of month and maximum tropopause pressure within the DI (in 20 hPa bins). We locate the maximum tropopause pressure in a given vertical profile as the top boundary of the dynamical tropopause defined by the 2 pvu isosurface. In the case of multiple tropopauses, if the 2-pvu isosurface is crossed again within 2 km below the top boundary, we select that tropopause pressure instead. Figure 2b shows that most cyclones have a tropopause pressure which is 100-200 hPa lower than the mean tropopause pressure, with a significant number of cyclones reaching much lower levels. Cyclones with the deepest stratospheric intrusions tend to occur most frequently in October-March. During the 8 years of our analysis period, we find that 32% of stratospheric intrusions in extratropical cyclones reach pressure altitudes below 500 hPa and 4.6% of cyclones reach pressures below 600 hPa. The

median tropopause altitude of DIs within cyclones is lowest in winter (DJF, 485 hPa, ~5.8 km) and highest in summer (JJA, 430 hPa, ~6.7 km). These results are consistent with *Wernli and Bourqui* [2002], who found that irreversible STT transport (defined as air parcel trajectories originating in the stratosphere with residence times greater than 4 days in the troposphere) occurs typically 0-200 hPa below the height of the climatological tropopause. Note that Figure 2b shows the depth of the DIs when they are associated with a cyclone, and does not track their fate after their stratospheric PV signature decays. Lagrangian climatologies tracking the subsequent mixing of DIs within the troposphere show that they frequently reach the lower troposphere in all seasons, but especially during winter and spring [*James et al.*, 2003; *Škerlak et al.*, 2014].

## 4 Ozone composites at 261 hPa and 464 hPa

### 4.1 Ozone composites at 261 hPa

Figure 4 shows composites of O<sub>3</sub> mixing ratios at 261 hPa for MLS, MERRA, MERRA-2 and GEOS-Chem. The 261 hPa level is the lowest level with valid MLS O<sub>3</sub> retrievals and we use it to examine O<sub>3</sub> concentrations in the lowermost stratosphere. The reanalyses and GEOS-Chem O<sub>3</sub> are interpolated to 261 hPa. In this Figure, we do not apply the MLS averaging kernel or horizontal sampling to the model fields, as we find that these effects change the results by less than 10%.

All composites show a consistent pattern featuring O<sub>3</sub> enhancements in the DI, 500 km to the southwest of the cyclone center, with O<sub>3</sub> mixing ratios of 170-220 ppbv for MLS, MERRA and MERRA-2, but lower values of 130-150 ppbv for GEOS-Chem (Figure 4). The O<sub>3</sub> anomalies,  $\Delta O_3$ , show the same pattern for all 4 composites and coincide with the location of the lowered tropopause, enhanced PV and decrease in H<sub>2</sub>O (Figure 3g-k). In the composites, the DI is ~1,000 km wide. The values of  $\Delta O_3$  in the DI are remarkably similar for MLS, MERRA and MERRA-2, reaching 25-75 ppbv above background (Figure 4, bottom panels). Weaker negative O<sub>3</sub> anomalies can also be seen in the WCB, to the east of the cyclone center, reflecting transport of O<sub>3</sub>-poor air both horizontally from lower latitudes, as well as vertically from lower altitudes within the WCB.

To quantify to seasonal variations in these O<sub>3</sub> enhancements, we identify the DI of each individual cyclone as the closed MERRA-2 261 hPa  $\Delta O_3$  contour where the following two conditions are met:  $\Delta O_3 > \frac{1}{2} \max(\Delta O_3)$  and  $\Delta H_2O < -25\%$ . The black contour in Figure 4g shows the area of the DI when we apply these criteria to the MERRA-2 composite. We extract the maximum O<sub>3</sub> and  $\Delta O_3$  for each cyclone within their DI, and then calculate the daily mean O<sub>3</sub> and  $\Delta O_3$  for all cyclones in the NH (there are typically ~4-6 cyclones on any given day in the NH, or 32-48/day over our 8-year period). Figure 5 shows the resulting seasonal cycles of the 261 hPa DI O<sub>3</sub> and  $\Delta O_3$  timeseries. Applying this selection criteria to individual cyclones allows for variations in the location of the DI and thus yields higher O<sub>3</sub> and  $\Delta O_3$  than the composites, in which slight horizontal variations lead to cancellations of positive and negative anomalies.

MLS O<sub>3</sub> in the DI maximizes at 400 ppbv in April and decreases to 180 ppbv in October-November, with an annual mean value of 292 ppbv (Figure 5a). This annual cycle follows the well-established seasonality of LS O<sub>3</sub> in the extratropical NH, with a slow buildup of O<sub>3</sub> throughout winter and early spring followed by dissipation in late spring and summer [*Logan*,



1999]. The winter/early spring build up is caused by strong poleward and downward transport of  $O_3$  combined with a long photochemical lifetime [e.g. *Holton et al.*, 1995]. The MERRA and MERRA-2 DI  $O_3$  mixing ratios display values that are very similar to MLS. GEOS-Chem  $O_3$  is 37% lower compared to the other 3 datasets and its maximum occurs one month earlier. This GEOS-Chem underestimate at 261 hPa is not limited to the cyclones, but extends to the entire NH extratropics at 200-300 hPa (not shown). We will discuss potential explanations for this underestimate in Section 4.2.

In terms of  $\Delta O_3$ , MLS, MERRA and MERRA-2 reach a maximum of 210 ppbv in April and a minimum of 100 ppbv in September-November (Figure 5b). MERRA has a narrower April maximum, resulting in a lower annual mean  $\Delta O_3$  of 136 ppbv compared to 153-154 ppbv for MLS and MERRA-2. Annually averaged, the 136-154 ppbv mean  $\Delta O_3$  in MLS, MERRA, and MERRA-2 results in a 85-115%  $O_3$  enhancement in the DI relative to background conditions. In GEOS-Chem, the DI enhancement in  $O_3$  is 45-50% lower compared to the other 3 datasets.

#### 4.2 Ozone composites at 464 hPa

The 464 hPa TES composite displays a distinct  $O_3$  enhancement in the DI reaching the middle troposphere within extratropical cyclones, with a 5-10 ppbv  $O_3$  enhancement in the DI (Figure 6ae). By examining the TES averaging kernel at 464 hPa for 40-60°N, we find that the mean contribution of levels above 300 hPa is less than 23% and less than 8% for levels above 200 hPa. Given this non-negligible contribution of lowermost stratospheric  $O_3$ , we apply the local TES averaging kernel and apriori to the reanalysis and modeling  $O_3$  profiles (Figure 6b-d).

The MERRA, MERRA-2 and GEOS-Chem composites show similar  $O_3$  patterns, with mean DI  $O_3$  enhancements of 5-10 ppbv for MERRA and MERRA-2, but only 2-5 ppbv for GEOS-Chem (Figure 6f-h). We identify the DI of each individual cyclone based on MERRA-2  $\Delta O_3$  closed contours at 464 hPa (following the same procedure as in section 4.1). The resulting seasonal cycle of daily 464 hPa DI  $O_3$  and  $\Delta O_3$  is shown in Figure 7. TES, MERRA and MERRA-2 reach maximum  $O_3$  mixing ratios of 95-100 ppbv in May, one month later than the maximum at 261 hPa. The GEOS-Chem underestimate of  $O_3$  mixing ratios at 464 hPa is particularly large between March and July, lacking the pronounced winter-spring  $O_3$  increase seen in the other datasets. The magnitude of the DI  $\Delta O_3$  at 464 hPa is similar in TES, MERRA and MERRA-2 with a maximum of 25-28 ppbv (35-40% enhancement relative to background) in April-May and a minimum of 12-14 ppbv (25% enhancement) in August-October.

A similar factor of two underestimate in the GEOS-Chem stratospheric  $O_3$  contribution was noted by *Hudman et al.* [2004] and *Liang et al.* [2007]. Off-line chemical transport models (CTMs) and trajectory models driven by assimilated winds appear to exhibit significantly larger cross-tropopause subtropical transport compared to transport computed from the parent free-running AGCM [*Douglass et al.*, 2003; *Schoeberl et al.*, 2003; *Tan et al.*, 2004; *Stohl et al.*, 2004]. This is caused by the lack of dynamic consistency in subsequent analysis fields that are generated by independent data assimilation cycles. The resulting “shocks” caused by data insertion are partially mitigated when time-averaged assimilated fields are used in CTMs [*Pawson et al.*, 2007], as done in GEOS-Chem, but significant differences remain. The excessive cross-tropopause transport in the subtropics is compensated by an underestimate in the magnitude of extratropical STE [*Hudman et al.*, 2004]. *Orbe et al.* [2017] compared a simulation

with the GMI CTM driven by MERRA analysis fields to a simulation with the online version of the GEOS-5 AGCM in “replay” mode, where the AGCM reads MERRA analysis fields every 6 hours, recomputes the analysis increments, which are then applied as a forcing to the meteorology. They found that in the winter extratropics, the concentrations of an idealized STE tracer were ~30% lower in the CTM compared to the AGCM (see Figure 2d in *Orbe et al.*, 2017). We conclude that the GEOS-Chem underestimate is consistent with a systematic underestimate of O<sub>3</sub> in the lowermost extratropical stratosphere due to errors in offline stratospheric transport driven by assimilated winds. Further investigating the detailed causes of these errors is beyond the scope of this paper and does not affect our results, which focus on the analysis of MERRA-2 O<sub>3</sub> fields in the following sections.

### 5 Three-dimensional O<sub>3</sub> and H<sub>2</sub>O composites with MERRA-2 fields

Figure 8 illustrates the annual composites of MERRA-2 O<sub>3</sub> and ΔO<sub>3</sub> at pressures between 400 hPa and 800 hPa. The DI composite O<sub>3</sub> mixing ratios are enhanced by 15-50% at 300 and 400 hPa, 3-6 % at 500-600 hPa, and <2% at 700 hPa. Within the DI, H<sub>2</sub>O decreases by 20-40% relative to background conditions.

In the WCB, east of the cyclone center, O<sub>3</sub> decreases by 2-5% and H<sub>2</sub>O increases by 10-50% relative to background conditions, as marine boundary layer O<sub>3</sub>-poor moist air is being lifted within the WCB [*Mari et al.*, 2000; *Grant et al.*, 2000]. WCBs in the western N. Atlantic and N. Pacific can draw from the polluted boundary layer, with elevated concentrations of O<sub>3</sub> and combustion tracers especially during spring and summer [e.g., *Cooper et al.*, 2002ab; *Miyazaki et al.*, 2003; *Liang et al.*, 2007; *Hegarty et al.*, 2010]. However, as most cyclones in the NH occur over clean oceanic regions (Figure 2a), the low-O<sub>3</sub> WCBs dominate our composites. In addition, because MERRA-2 does not contain detailed tropospheric O<sub>3</sub> chemistry it likely underestimates the WCB export of high O<sub>3</sub> from the polluted continental boundary layer.

As the O<sub>3</sub>-rich DI descends, the maximum O<sub>3</sub> enhancements propagates slightly to the southwest of the cyclone center. The DI forms a coherent and vertically aligned structure, wrapping around cyclonically with the WCB (Figure 8). It appears that in the composites, the two dominant branches of the DI and WCB are branches B and C, respectively (Figure 1). This corresponds to the LC2 cyclone life cycle, with a very deep cutoff vortex. Using passive tracers in idealized numerical experiments, *Polvani and Elser* [2007] found that STT mass transport was 50% greater in the LC2 life cycle compared to the LC1 cycle, as the relatively large LC2 vortices provide an efficient mixing zone between stratospheric and tropospheric air. The LC1 structure forms narrow streamers (~200 km) that will split and/or roll-up [*Appenzeller and Davies*, 1992] and would thus not be as prominent in our composites.

For each cyclone and each pressure level, we identify the DI based on ΔO<sub>3</sub> and ΔH<sub>2</sub>O (as in Section 4) and extract the maximum O<sub>3</sub> and ΔO<sub>3</sub>. Figure 9 shows the resulting seasonal mean vertical profiles. The O<sub>3</sub> enhancement within cyclones exceeds 100 ppbv throughout the lowermost stratosphere (<250 hPa). The largest DI O<sub>3</sub> enhancement relative to background conditions reaches 100-130% at 250-300 hPa (Figure 9bc). The DI O<sub>3</sub> enhancement remains significant at pressure altitudes below 500 hPa, with contributions of 6-20 ppbv (15-30%). Summer and fall extratropical cyclones result in weaker ΔO<sub>3</sub> relative to winter and spring. *Knowland et al.* [2015] composite intense spring storms over the N. Atlantic and N. Pacific using

the MACC reanalysis, finding DI O<sub>3</sub> enhancements of 100-150 ppbv at 300 hPa and 10-25 ppbv at 500 hPa (their Figure 13) similar to our results.

How much of the O<sub>3</sub> enhancement in the DI originates from the lowermost stratosphere as opposed to the upper troposphere? How much mixing has taken place as the DI descends within the troposphere? To try to answer these questions, we use the GEOS-Chem simulation to examine the fraction of  $\Delta\text{O}_3$  that is explained by an enhancement in the tagged stratospheric O<sub>3</sub> tracer (dashed lines in Figure 9c). As GEOS-Chem underestimates stratospheric O<sub>3</sub> enhancements by a factor of 2 (Sect. 4), we correct for this by doubling the concentrations of the stratospheric O<sub>3</sub> tracer. During winter and spring, we find that stratospheric O<sub>3</sub> accounts for 80-90% of  $\Delta\text{O}_3$  at 500 hPa, 65-75% at 600 hPa, and 25-40% at 800 hPa. Thus, for these seasons, the DI keeps its stratospheric characteristic until 400-500 hPa, below which mixing with tropospheric air occurs. During summer and fall, the stratospheric contribution at 500 hPa is ~40%, and thus O<sub>3</sub>-rich upper tropospheric air dominates  $\Delta\text{O}_3$  in DIs because descent of stratospheric O<sub>3</sub> reaches low altitudes less frequently (Figure 2b).

## 6 Dry intrusions contribution to stratosphere-troposphere exchange of O<sub>3</sub>

We now quantify the role of extratropical cyclones in the STE transport of O<sub>3</sub> using MERRA-2. We focus here on STT transport in the DI of extratropical cyclones and will not examine the troposphere-to-stratosphere transport (TST) occurring within the WCB [e.g., *Wernli and Bourqui*, 2002]. The MERRA-2 reanalysis represents well near tropopause O<sub>3</sub> variability, and is particularly robust in the lowermost stratosphere because of the assimilation of MLS. However, as noted earlier, the lack of detailed tropospheric chemistry results in a low bias in the UT making MERRA-2 O<sub>3</sub> not as useful to assess TST transport.

Here, we make the following assumption: for each daily 4,000 km × 4,000 km cyclone-centric grid, we assume that all the stratospheric O<sub>3</sub> between the local 2 pvu dynamical tropopause and the level 75 hPa below the climatological dynamical tropopause will be irreversibly mixed into the troposphere. We calculate the climatological dynamical tropopause as the 2005-2012 daily mean tropopause to which we apply a 60-day running mean and a 15° wide boxcar smoothing. The NH extratropical dynamical tropopause is typically around 300 hPa (black line in Figure 2d). If we define the entire DI as being bounded by the locally lowered dynamical tropopause and the climatological tropopause of ~300 hPa, then about 15% of the O<sub>3</sub> mass in the DI is below 375 hPa. We assume that this fraction is irreversibly mixed in the troposphere for each individual cyclone identified on each day. Our definition of this upper level of the mixing zone (~375 hPa) tries to eliminate shallow STT transport within DIs [*Stohl et al.*, 2003], focusing on the deeper part of the DI that is most likely to be irreversibly mixed into the troposphere via diabatic processes [*Lamarque and Hess*, 1994; *Rood et al.*, 1997]. We will examine the sensitivity of our results to the choice of different mixing zones in Section 6.3.

### 6.1 Composites of O<sub>3</sub> stratosphere-to-troposphere flux

The composite of O<sub>3</sub> STT flux for all the cyclones in 2005-2012 (Figure 10a) shows the largest flux occurring to the southwest of the cyclone center, co-located with the O<sub>3</sub> enhancement and lowered tropopause (Figure 3). Integrating over the composite 4,000×4,000 km<sup>2</sup> domain, we find that DIs lead to a mean STT flux per cyclone of 0.059 Tg O<sub>3</sub> d<sup>-1</sup> (Figure 10a). This estimate

is broadly consistent with published case studies. *Beekman et al.* [1997] summarize estimates of STT  $O_3$  fluxes within tropopause folds from six published case studies for different seasons and methodologies, finding a mean flux of  $0.054 \text{ Tg } O_3 \text{ d}^{-1}$ , with values ranging from  $0.01 \text{ Tg } O_3 \text{ d}^{-1}$  [Lamarque and Hess, 1994] to  $0.082 \text{ Tg } O_3 \text{ d}^{-1}$  [Ancellet et al., 1991; Ebel et al., 1996]. Based on lagrangian trajectories, *Cooper et al.* [2004] calculate a  $0.15 \text{ Tg } O_3 \text{ d}^{-1}$  STT flux for a deep DI over the Pacific Ocean. Using ground-based  $O_3$  lidar profiles, *Kuang et al.* [2012] infer a  $0.035\text{--}0.055 \text{ Tg } O_3 \text{ d}^{-1}$  STT flux associated with a spring cutoff cyclone over Alabama.

*Reutter et al.* [2015] coupled a sophisticated cyclone identification methodology with a lagrangian model to quantify the exchange of air across the extratropical tropopause in the vicinity of North Atlantic midlatitude cyclones with the ERA-Interim reanalysis dataset for 1979-2011. Their cyclone centric composites indicate that most STT transport of air occurs south-west of the cyclone center during the intensification phase, then moves to the south of the cyclone center when the cyclones reach their minimum SLP, with a pattern very similar to our composite of STT mass flux (Figure 10b). We find an average STT mass flux of  $0.45 \text{ Tg air d}^{-1}$  corresponding to  $325 \text{ kg km}^{-2} \text{ s}^{-1}$  per cyclone in the NH. This is similar to the average mass flux of  $340.7 \text{ kg km}^{-2} \text{ s}^{-1}$  per cyclone over the N. Atlantic reported by *Reutter et al.* [2015].

Figure 11 (top panels) examines the seasonal variability in  $O_3$  STT associated with the DI of cyclones. The winter and spring composites display the strongest mean STT fluxes, with values of  $\sim 0.07 \text{ Tg } O_3 \text{ d}^{-1}$ , nearly twice as large as the  $\sim 0.04 \text{ Tg } O_3 \text{ d}^{-1}$  for summer and fall cyclones (Figure 11a-d). For each season, we further examine how the STT  $O_3$  flux varies with cyclone strength. Depending on the property studied, different metrics have been used as proxies of cyclone intensity: minimum SLP, windspeed, PV, local laplacian of SLP, central vorticity, circulation [e.g., *Johnson and Vizee*, 1981; *Sinclair*, 1995, 1997; *Wang et al.*, 2006; *Field and Wood*, 2007]. We examined the dependence of STT  $O_3$  flux on the first three of these proxies, finding the strongest dependence for 300 hPa windspeed ( $u_{300\text{hPa}}$ , defined as the maximum windspeed in the southern quadrants of the cyclone, see Figure 3c). The STT  $O_3$  flux increases rapidly with increasing  $u_{300\text{hPa}}$  for all seasons (Figure 11 e-h). During winter as  $u_{300\text{hPa}}$  increases from  $30\text{--}40 \text{ m s}^{-1}$  to  $100\text{--}110 \text{ m s}^{-1}$ , the STT flux increases from  $0.01\text{--}0.07 \text{ Tg } O_3 \text{ d}^{-1}$  (upper and lower quartiles) to  $0.11\text{--}0.24 \text{ Tg } O_3 \text{ d}^{-1}$  (Figure 11f). To first order,  $u_{300\text{hPa}}$  appears to be a good proxy to determine the magnitude of the STT  $O_3$  flux in DIs. We find that the DI  $\Delta O_3$  at 261 hPa and 464 hPa also display a strong dependence on  $u_{300\text{hPa}}$  (see Figures S2-5), which indicates that stronger cyclones bring down stratospheric air from higher altitudes and hence larger  $O_3$  mixing ratios, or that the descent is faster and less mixing occurs [Johnson and Vizee, 1981]. We found a weaker dependence of the STT  $O_3$  flux on SLP and 300 hPa PV (Figure S1), possibly because these quantities have strong latitudinal gradients.

## 6.2 Temporal and spatial variability of $O_3$ STT flux from cyclones

We show the daily mean  $O_3$  total STT flux from all NH cyclones for 2005-2012 in Figure 10c. The resulting annual cycle of the DI STT maximizes in March to a value of  $0.5 \text{ Tg } O_3 \text{ d}^{-1}$  and decreases gradually to reach a minimum of  $0.1 \text{ Tg } O_3 \text{ d}^{-1}$  in July-August (Figure 10c). This annual cycle closely follows mass transport induced by the lowering of the DI depth in winter

1 and spring (Figure 2d), combined with the broad springtime peak in the lowermost stratospheric  
2 O<sub>3</sub> mixing ratio (Figure 5a). We find that DIs contribute to an annual flux of 119 Tg O<sub>3</sub> yr<sup>-1</sup>.

3 We compare this STT flux due to cyclones to the extratropical NH STT flux on the  
4 tropopause, diagnosed using the mass conservation approach of *Appenzeller et al.* [1996]. In this  
5 approach, the extratropical STT O<sub>3</sub> flux across the tropopause is the sum of the flow into the LS  
6 and the time rate of change of the O<sub>3</sub> mass in the LS. Following *Shoeberl* [2004] and *Olsen et al.*  
7 [2004], we assume that the LS is bounded by the 380 K potential temperature surface and the  
8 dynamical tropopause, and use the MERRA-2 heating rates and O<sub>3</sub> mixing ratios on the 380 K  
9 potential temperature surface to calculate the flow into the LS. This results in a multiyear (2005-  
10 2012) extratropical STT flux of 492 Tg yr<sup>-1</sup>: 281 Tg yr<sup>-1</sup> in the NH and 211 Tg yr<sup>-1</sup> in the SH.  
11 This is very close to the values reported by *Olsen et al.* [2013] for 2005-2010 (NH: 275 Tg yr<sup>-1</sup>;  
12 SH: 214 Tg yr<sup>-1</sup>) based on MERRA heating rates and MLS O<sub>3</sub> observations. For 2001-2005, *Hsu*  
13 *and Prather* [2009] report a best estimate of 290 Tg yr<sup>-1</sup> in the NH and 225 Tg yr<sup>-1</sup> in the SH.  
14 *Gottelman et al.* [1997] report a total STE flux of 510 Tg yr<sup>-1</sup>. The annual cycle of the MERRA-2  
15 extratropical NH STT flux is consistent with these previous studies, with a broad maximum in  
16 spring and minimum in fall (Figure 10c).

17 We find that transport within extratropical cyclones accounts for 42% of the NH STT O<sub>3</sub>  
18 flux. The largest contributions of cyclones to the total STT O<sub>3</sub> flux occur during winter (47%,  
19 37.4 Tg) and fall (71%, 22.7 Tg). During spring, cyclones account for 41% (43.2 Tg) of the NH  
20 STT flux. By averaging 6 case studies of tropopause folds, *Beekman et al.* [1997] calculate a  
21 mean STT O<sub>3</sub> flux of  $5.7 \times 10^{10}$  molecules O<sub>3</sub> cm<sup>-2</sup> s<sup>-1</sup> in the NH, or ~140 Tg O<sub>3</sub> yr<sup>-1</sup> for 30-60°N.  
22 *Cooper et al.* [2004] extrapolated their study of one DI event during spring to estimate a 28 Tg  
23 O<sub>3</sub> flux for spring in the NH. *Reutter et al.* [2015] find that 50-60% of the STT mass flux in the  
24 North Atlantic Ocean occurs in the vicinity of cyclones. Our findings are thus in broad  
25 agreement with these past studies and provide a more systematic estimate of the STT O<sub>3</sub> flux due  
26 to extratropical cyclones for the entire NH.

27 Figure 11i shows that the daily DI O<sub>3</sub> STT flux associated with extratropical cyclones  
28 displays very large day-to-day variability, with an interquartile range of -55% to +95% relative  
29 to the median. There is also some significant interannual variability, with the DI O<sub>3</sub> STT flux  
30 varying between 136 Tg yr<sup>-1</sup> and 107 Tg yr<sup>-1</sup> for the 8-year period we examined. These two  
31 extremes also correspond to the years with the largest (2010: 303 Tg yr<sup>-1</sup>) and lowest (2007: 262  
32 Tg yr<sup>-1</sup>) extratropical NH O<sub>3</sub> flux. Variability in both the El Niño/Southern Oscillation (ENSO)  
33 and the stratospheric Quasi-Biennial Oscillation (QBO) have been shown to modulate  
34 stratospheric circulation and the STE O<sub>3</sub> flux [e.g., *Baldwin et al.*, 2001; *Zheng and Pyle*, 2005;  
35 *Hsu and Prather*, 2009]. *Neu et al.* [2014] showed that the 2007-2008 La Niña/westerly shear  
36 QBO was associated with a weaker stratospheric overturning circulation and decreased O<sub>3</sub> STE,  
37 while the 2009-2010 El Niño/easterly shear QBO led to a stronger stratospheric circulation and  
38 increased O<sub>3</sub> STE [*Neu et al.*, 2014]. Our results show a 15% enhancement in O<sub>3</sub> STE for the  
39 winter and spring of 2009-2010 compared to 2007-2008 (Figure 11i).

40 Figure 12 shows that STT from DIs is concentrated in the Pacific and Atlantic storm  
41 track regions, extending from Japan to the North American west coast and from the northeast  
42 U.S. to northern Europe. During winter, STT is largest 30-40°N, shifting to 35-45°N in spring,  
43 and 40-50°N in summer and fall. Some of the STT occurs over land, in particular during winter

over Alaska, Eastern N. America, and over Northern Europe. During spring, there is a particularly strong O<sub>3</sub> STT flux over the southwest U.S., where it has been shown to influence surface O<sub>3</sub> concentrations [e.g., *Langford et al.*, 2009; *Lefohn et al.*, 2011; *Lin et al.*, 2012, 2015]. This overall spatial and seasonal pattern is similar to that obtained using lagrangian methods [e.g., *Wernli and Bourqui*, 2002; *Sprenger and Wernli*, 2003; *Škerlak et al.*, 2014; *Reutter et al.*, 2015] and tropospheric O<sub>3</sub> mass balance in a CTM [*Hsu et al.*, 2005]. In particular, with an entirely different approach (using tropopause heating rates from a general circulation model and O<sub>3</sub> fields in a chemical transport model), *Olsen et al.* [2004] finds a very strong diabatic downward flux in the N. Atlantic and N. Pacific storm tracks. They report a stratospheric component of this diabatic flux of 133 Tg O<sub>3</sub> yr<sup>-1</sup> in the NH, very similar to our results, further evidence of diabatic processes in cyclone-mediated tropopause folds as a major mechanism for O<sub>3</sub> STT.

### 6.3 Sensitivity of cyclone O<sub>3</sub> STT flux estimate to assumptions about mixing zone

As noted in the introduction, assessing the contribution of extratropical cyclones to STT transport is an inherently difficult problem because of the multiple physical processes that can lead to mixing of stratospheric air into the troposphere on various spatiotemporal scales. Thus, different approaches quantifying extratropical cyclone STT fluxes tend to have their own assumptions and limitations, whether it be idealized simulations [*Bush and Peltier*, 1994; *Polvani and Esler*, 2007], generalization of a few case studies [*Beekman et al.*, 1997; *Cooper et al.*, 2004], or more systematic Lagrangian studies, which require criteria about irreversible mixing based on residence time and/or vertical extent of transport [e.g., *Reutter et al.*, 2015; *Raveh-Rubin*, 2017].

Our approach also has its limitations. In particular, the calculated STT flux for extratropical cyclones is sensitive to the upper pressure boundary we choose to demarcate irreversible transport of O<sub>3</sub> within the DI. Using 75 hPa below the climatological tropopause and thus assuming that 15% of the O<sub>3</sub> mass of the DI is irreversibly mixed, we found that DIs contribute to an annual flux of 119 Tg O<sub>3</sub> yr<sup>-1</sup> (Figures 10-12). If instead we choose 60 hPa or 100 hPa below the climatological tropopause (assuming that 22% or 8% of the DI is irreversibly mixed), we calculate STT fluxes of 174 Tg O<sub>3</sub> yr<sup>-1</sup> and 62 Tg O<sub>3</sub> yr<sup>-1</sup>, respectively (see Figure S4). Taking these two mixing zone assumptions as upper and lower bounds on our estimate, we find that extratropical cyclones account for 42±20% of the NH STT flux.

Another limitation of our analysis is that we do not track individual cyclones over their lifecycle. The strength of STT transport within extratropical cyclones varies over their typical 1 week lifecycle, but tends to be strongest during their mature phase (24 hour window around the time of maximum intensity), which accounts for 50-70% of their overall STT [*Reutter et al.*, 2015]. We calculate the daily STT flux for a moving cyclone as it evolves over several days without directly taking into account its lifecycle stage. The only way this is accounted for is that the location of the 2-pvu dynamical tropopause will vary over that lifecycle, and hence our resulting O<sub>3</sub> flux will also vary with time.

## 7 Summary and concluding remarks

Our analysis presents the first systematic assessment of observationally constrained O<sub>3</sub> enhancements and O<sub>3</sub> STT fluxes associated with the dry intrusions of extratropical cyclones in

the northern hemisphere. We show that the cyclone-centric composites provide a useful framework to test STT O<sub>3</sub> fluxes calculated with CTMs and GCMs, thus allowing to quantify potential biases due to transport or O<sub>3</sub> concentrations. The composites of 15,978 cyclones in the NH for 2005-2012 show a well-defined ~1,000 km wide DI to the southwest of the cyclone center, with enhancements in O<sub>3</sub> and potential vorticity, co-located with lower H<sub>2</sub>O and depressed tropopause altitude. Vertically, most DIs reach pressures between 400 and 600 hPa, with the deepest DIs occurring in winter and spring. MLS observations at 261 hPa in the lowermost stratosphere display mean DI O<sub>3</sub> enhancements of 154 ppbv (115% enhancements relative to background), reaching an April maximum of 210 ppbv. TES observations at 464 hPa reach an April maximum of 27 ppbv O<sub>3</sub> enhancement in DIs, 35% above background. While MERRA and MERRA-2 reanalyses capture these satellite observations very well, O<sub>3</sub> enhancements in GEOS-Chem are a factor of 2 too low. This underestimate likely reflects errors in offline stratospheric transport driven by assimilated winds in the CTM as reported by previous studies [e.g., *Tan et al.*, 2004; *Hudman et al.*, 2004; *Pawson et al.*, 2007; *Orbe et al.*, 2017].

Using the MERRA-2 O<sub>3</sub> and H<sub>2</sub>O composites, we find that the DI forms a coherent vertically-aligned vortex from 300 hPa to 800 hPa as it wraps cyclonically around the WCB. Seasonally, the vertical O<sub>3</sub> enhancements in DIs are largest at 300 hPa, leading to a doubling of O<sub>3</sub> mixing ratios relative to background conditions. The O<sub>3</sub> enhancement in the DI at lower altitudes is strongest in winter and spring, with a 6-20 ppbv enhancement (15-30%) at levels below 500 hPa.

We find that DIs account for an annual mean NH STT flux of 119 Tg O<sub>3</sub> yr<sup>-1</sup>, which constitutes 42% of the extratropical STT O<sub>3</sub> flux. This estimate relies on the assumption that on any given day 15% of the O<sub>3</sub> mass in the DI is irreversibly mixed in the troposphere. We assess an uncertainty range of ±56 Tg O<sub>3</sub> yr<sup>-1</sup> on the DI STT flux by varying this assumption. The STT O<sub>3</sub> flux from cyclones increases rapidly with increasing cyclone intensity, which we characterize by the maximum 300 hPa westerly windspeed in the jet. This link to the jet windspeed is consistent with the quasigeostrophic dynamical theory of cyclone development: increasing upper level jet windspeed leads to more vertical wind shear, stronger temperature gradient, and hence strong static stability with stronger and deeper intrusions [e.g., *Danielsen et al.*, 1968; *Wallace and Hobbs*, 2006].

The Brewer-Dobson circulation is expected to strengthen with increasing greenhouse gases [*Butchard et al.*, 2006], resulting in larger O<sub>3</sub> STE [*Collins et al.*, 2003; *Sudo et al.*, 2003]. The Atmospheric Chemistry and Climate Model Intercomparison Project (ACCMIP) predicts a 40-150% increase in O<sub>3</sub> STE by the end of the 21<sup>st</sup> century for the RCP8.5 scenario [*Kawase et al.*, 2011; *Young et al.*, 2013]. Part of this increase is due to the recovery of stratospheric O<sub>3</sub> as halogen levels decrease in the future [e.g., *Hegglin and Shepherd*, 2009; *Eyring et al.*, 2010]. The response of extratropical cyclones to changing climate conditions is less clear because of the opposing effects of a weaker meridional temperature gradient and increased moisture [*Shaw et al.*, 2016, and references therein]. The most consistent prediction among climate models for 2100 is a poleward shift in the NH storm tracks during fall, but weaker and less robust shifts during other seasons [*Simpson et al.*, 2014]. We might thus expect the fall pattern of O<sub>3</sub> STT flux in Figure 12d to strengthen and shift poleward by a few degrees latitude. During winter, climate models tend to predict a reduction of the tilt of the N. Atlantic storm track accompanied by an eastward extension into Europe [*Zappa et al.*, 2013]. For the Pacific winter storm track,

predictions are for a poleward shift in the west Pacific and an equatorward shift in the East Pacific, together with an increase in extratropical cyclones over the N. American west coast [Simpson *et al.*, 2014; Chang *et al.*, 2015]. This suggests more frequent wintertime O<sub>3</sub> DIs over the western U.S. and western Europe. More generally, climate models predict poleward increase of storm track activity, but in the NH most of this strengthening is limited to the UT/LS and the overall frequency of extratropical cyclones would decrease [Chang *et al.*, 2012]. This implies that while fewer extratropical cyclones might occur in a future warmer climate, their DI would tend to bring down more stratospheric O<sub>3</sub> per cyclone.

## Acknowledgments

This work was supported by funding from the NASA Atmospheric Composition Modeling and Analysis Program under award NNX11AL74G. We acknowledge the MLS, TES, and AIRS mission scientists and science teams for the production of the data used in this analysis. We also acknowledge NASA Goddard's Global Modeling and Assimilation Office for producing and validating the MERRA and MERRA-2 products. The satellite observations used in this study can be accessed as follows: MLS (<https://mls.jpl.nasa.gov/data/overview.php>), TES (<https://tes.jpl.nasa.gov/data/>), AIRS ([https://airs.jpl.nasa.gov/data/get\\_data](https://airs.jpl.nasa.gov/data/get_data)). The MERRA and MERRA-2 fields are available at <https://gmao.gsfc.nasa.gov/reanalysis/>.

## References

- Ancelet, G., J. Pelon, M. Beekmann, A. Papagiannis, and G. Mégie (1991), Ground based lidar studies of ozone exchanges between the stratosphere and the troposphere, *J. Geophys. Res.*, 96, 22401–22421, doi:10.1029/91JD02385.
- Appenzeller, C., and H.C. Davies (1992), Structure of stratospheric intrusions into the troposphere, *Nature*, 358, 570–572, doi:10.1038/358570a0.
- Appenzeller, C., J. R. Holton, and K. Rosenlof (1996), Seasonal variation of mass transport across the tropopause, *J. Geophys. Res.*, 101, 15,071–15,078, doi: 10.1029/96JD00821.
- Aumann, H. H., et al. (2003), AIRS/AMSU/HSB on the aqua mission: Design, science objectives, data products, and processing systems, *IEEE Trans. Geosci. Remote Sens.*, 41(2), 253–264, doi:10.1109/tgrs.2002.808356.
- Baldwin, M. P. et al (2001), The Quasi-Biennial Oscillation, *Rev. Geophys.*, 39, 179–229, doi : 10.1029/1999RG000073.
- Beekmann, M., et al. (1997), Regional and global tropopause fold occurrence and related ozone flux across the tropopause, *J. Atmos. Chem.*, 28, 29–44, doi:10.1023/A:1005897314623.
- Beer, R. et al. (2006), TES on the Aura mission: Scientific objectives, measurements, and analysis overview, *IEEE Trans. Geosci. Remote Sens.*, 44, 1102–1105, doi: 10.1109/TGRS.2005.863716.
- Bey, I., D. J. Jacob, R. M. Yantosca, J. A. Logan, B. Field, A. M. Fiore, Q. Liu, L. J. Mickley, and M. Schultz (2001), Global modeling of tropospheric chemistry with assimilated meteorology: Model description and evaluation, *J. Geophys. Res.*, 106, 23,073–23,096, doi:10.1029/2001JD000807.



- Bhartia, P. K., C. G. Wellemeyer, S.L. Taylor, N. Nath, and A. Gopalan (2004), Solar Backscatter Ultraviolet (SBUV) Version 8 profile algorithm, in *Proceedings of the XX Quadrennial Ozone Symposium*, edited by C. Zerefos, pp. 295–296, Univ. of Athens, Greece.
- Browning, K. A., and N. M. Roberts (1994), Structure of a frontal cyclone, *Q. J. R. Meteorol. Soc.*, 120, 1535–1557.
- Browning, K. A., (1997), The dry intrusion perspective of extra-tropical cyclone development, *Meteorol. Appl.*, 4, 317–324.
- Bush, A. B. G. and W. R. Peltier (1994), Tropopause folds and synoptic scale baroclinic wave life cycles, *J. Atmos. Sci.*, 51, 1581–1604, doi:10.1175/1520-0469.
- Butchart, N., A. A. Scaife, M. S. Bourqui, J. de Grandpré, J., S. H. E. Hare, J. A. Kettleborough, U. Langematz, E. Manzini, F. Sassi, K. Shibata, D. T. Shindell, and M. Sigmond (2006), Simulations of anthropogenic change in the strength of the Brewer–Dobson circulation, *Clim. Dynam.*, 27, 727–741, doi:10.1007/s00382-006-0162-4.
- Carlson, T. N. (1980), Airflow through midlatitude cyclones and the comma cloud pattern, *Mon. Weather Rev.*, 108, 1498– 1509.
- Catto, J. L., L. C. Shaffrey, and K. L. Hodges (2010), Can climate models capture the structure of extratropical cyclones? *J. Climate*, 23, 1621–1635, doi: 10.1175/2009JCLI3318.1.
- Chang, E. K. M., and S. Song (2006), The Seasonal Cycles in the Distribution of Precipitation around Cyclones in the Western North Pacific and Atlantic, *J. Atmos. Sci.*, 63, 815–839, doi:10.1175/JAS3661.1.
- Chang, E. K. M., Y. Guo, and X. Xia (2012), CMIP5 multimodel ensemble projection of storm track change under global warming, *J. Geophys. Res.*, 117, D23118, doi:10.1029/2012JD018578.
- Chang, E. K. M., C. Zheng, P. Lanigan, A. M. W. Yau, and J. D. Neelin (2015), Significant modulation of variability and projected change in California winter precipitation by extratropical cyclone activity, *Geophys. Res. Lett.*, 42, 5983–5991, doi:10.1002/2015GL064424.
- Cho, J. Y. N., et al. (1999), Observations of convective and dynamical instabilities in tropopause folds and their contribution to stratosphere-troposphere exchange, *J. Geophys. Res.*, 104(D17), 21549–21568, doi:10.1029/1999JD900430.
- Collins, W. J., R. G. Derwent, B. Garnier, C. E. Johnson, M. G. Sanderson, and D. S. Stevenson (2003), Effect of stratosphere troposphere exchange on the future tropospheric ozone trend, *J. Geophys. Res.*, 108, 8528, doi:10.1029/2002JD002617.
- Cooper, O. R., J. L. Moody, J. C. Davenport, S. J. Oltmans, B. J. Johnson, P. B. Shepson, X. Chen, and J. T. Merrill (1998), The influence of springtime weather systems on vertical ozone distributions over three North American sites, *J. Geophys. Res.*, 103, 22,001–22,013, doi:10.1029/98JD01801.
- Cooper, O. R., J. L. Moody, D. D. Parrish, M. Trainer, T. B. Ryerson, J. S. Holloway, G. Hübler, F. C. Fehsenfeld, and M. J. Evans (2002a), Trace gas composition of midlatitude

- cyclones over the western north Atlantic ocean: A conceptual model, *J. Geophys. Res.*, 107(D7), doi:10.1029/2001JD000901.
- Cooper, O. R., J. L. Moody, D. D. Parrish, M. Trainer, J. S. Holloway, G. Hübler, F. C. Fehsenfeld, and A. Stohl (2002b), Trace gas composition of midlatitude cyclones over the western North Atlantic Ocean: A seasonal comparison of O<sub>3</sub> and CO, *J. Geophys. Res.*, 107 (D7), doi:10.1029/2001JD000902.
- Cooper, O. R., R. S. Gao, D. Tarasick, T. Leblan, and C. Sweeney (2012), Long-term ozone trends at rural ozone monitoring sites across the United States, 1990-2010, *J. Geophys. Res.*, 117, D22307, doi:10.1029/2012JD018261.
- Cooper, O., R., et al. (2004), On the life cycle of a stratospheric intrusion and its dispersion into polluted warm conveyor belts, *J. Geophys. Res.*, 109, D23S09, doi:10.1029/2003JD004006.
- Dacre, H. F., and S. L. Gray (2009), The spatial distribution and evolution characteristics of North Atlantic cyclones, *Mon. Wea. Rev.*, 137, 99–115, doi:10.1175/2008MWR2491.1.
- Danielsen, E. F. (1968), Stratospheric-tropospheric exchange based on radioactivity, ozone and potential vorticity, *J. Atmos. Sci.*, 25, 502–518, doi:10.1175/1520-0469.
- Danielsen, E. F. (1980), Stratospheric source for unexpectedly large values of ozone measured over the Pacific Ocean during Gametag, August 1977, *J. Geophys. Res.*, 85, 401–412, doi: 10.1029/JC085iC01p00401.
- Douglass, A. R., C. J. Weaver, R. B. Rood, and L. Coy (1996), A three-dimensional simulation of the ozone annual cycle using winds from a data assimilation system, *J. Geophys. Res.*, 101(D1), 1463–1474, doi:10.1029/95JD02601.
- Douglass, A. R., M. R. Schoeberl, R. B. Rood, and S. Pawson (2003), Evaluation of transport in the lower tropical stratosphere in a global chemistry and transport model, *J. Geophys. Res.*, 108, 4259, doi:10.1029/2002JD002696.
- Ebel, A., H. Elbern, J. Hendricks, and R. Meyer (1996), Stratosphere-troposphere exchange and its impact on the structure of the lower stratosphere, *J. Geomag. Geoelectr.*, 48, 135–144.
- Eyring, V. et al. (2010), Multimodel assessment of stratospheric ozone return dates and ozone recovery in CCMVal-2 models, *Atmos. Chem. Phys.*, 10, 9451–9472, doi:10.5194/acp-10-9451-2010.
- Field, P. R., and R. Wood (2007), Precipitation and Cloud Structure in Midlatitude Cyclones, *J. Climate*, 20, 233–254, doi:10.1175/JCLI3998.1.
- Field, P. R., A. Gettelman, R. Neale, R. Wood, P. J. Rasch, and H. Morrison (2008), Midlatitude cyclone compositing to constrain climate model behavior using satellite observations, *J. Climate*, 21, 5887–5903, doi:10.1175/2008JCLI2235.1.
- Frederick, J.E., R. P. Cebula, and D. F. Heath (1986), Instrument characterization for the detection of long-term changes in stratospheric ozone: An analysis of the SBUV/2 radiometer, *J. Atmos. Oceanic Technol.*, 3, 472-480, doi: 10.1175/1520-0426(1986)003<0472:ICFTDO>2.0.CO;2.

- 1 Fusco, A. C. and J. A. Logan (2003), Analysis of 1970–1995 trends in tropospheric ozone at  
2 Northern Hemisphere midlatitudes with the GEOS-CHEM model, *J. Geophys. Res.*, 108,  
3 4449, doi:10.1029/2002JD002742.
- 4 Gelaro, R., W. McCarty, M.J. Suárez, R. Todling, A. Molod, L. Takacs, C. Randles, A.  
5 Darmenov, M.G. Bosilovich, R. Reichle, K. Wargan, L. Coy, R. Cullather, C. Draper, S.  
6 Akella, V. Buchard, A. Conaty, A. da Silva, W. Gu, G. Kim, R. Koster, R. Lucchesi, D.  
7 Merkova, J.E. Nielsen, G. Partyka, S. Pawson, W. Putman, M. Rienecker, S.D. Schubert,  
8 M. Sienkiewicz, and B. Zhao (2017), The Modern-Era Retrospective Analysis for  
9 Research and Applications, Version 2 (MERRA-2), *J. Climate*, 30, 5419–5454,  
10 doi:10.1175/JCLI-D-16-0758.1
- 11 Gettelman, A., J. R. Holton, and K. H. Rosenlof (1997), Mass fluxes of O<sub>3</sub>, CH<sub>4</sub>, N<sub>2</sub>O and  
12 CF<sub>2</sub>Cl<sub>2</sub> in the lower stratosphere calculated from observational data, *J. Geophys. Res.*,  
13 102(D15), 19149–19159, doi:10.1029/97JD01014.
- 14 Global Modeling and Assimilation Office (GMAO)(2015a), MERRA-2 inst3\_3d\_asm\_Np: 3d,3-  
15 Hourly,Instantaneous,Pressure-Level,Assimilation,Assimilated Meteorological Fields  
16 V5.12.4, Greenbelt, MD, USA, Goddard Earth Sciences Data and Information Services  
17 Center (GES DISC), Accessed June 2016, 10.5067/QBZ6MG944HW0
- 18 Global Modeling and Assimilation Office (GMAO)(2015b), MERRA-2 inst3\_3d\_chm\_Nv: 3d,3-  
19 Hourly,Instantaneous,Model-Level,Assimilation,Carbon Monoxide and Ozone Mixing  
20 Ratio V5.12.4, Greenbelt, MD, USA, Goddard Earth Sciences Data and Information  
21 Services Center (GES DISC), Accessed June 2016, 10.5067/HO9OVZWF3KW2
- 22 Global Modeling and Assimilation Office (GMAO)(2015c), MERRA-2 tavg3\_3d\_tdt\_Np: 3d,3-  
23 Hourly,Time-Averaged,Pressure-Level,Assimilation,Temperature Tendencies V5.12.4,  
24 Greenbelt, MD, USA, Goddard Earth Sciences Data and Information Services Center  
25 (GES DISC), Accessed June 2016, 10.5067/9NCR9DDDOPFI
- 26 Global Modeling and Assimilation Office (GMAO)(2015d), MERRA-2 tavg1\_2d\_slv\_Nx: 2d,1-  
27 Hourly,Time-Averaged,Single-Level,Assimilation,Single-Level Diagnostics V5.12.4,  
28 Greenbelt, MD, USA, Goddard Earth Sciences Data and Information Services Center  
29 (GES DISC), Accessed June 2016, 10.5067/VJAFPLI1CSIV
- 30 Global Modeling and Assimilation Office (GMAO)(2015e), MERRA-2 tavg1\_2d\_flx\_Nx: 2d,1-  
31 Hourly,Time-Averaged,Single-Level,Assimilation,Surface Flux Diagnostics V5.12.4,  
32 Greenbelt, MD, USA, Goddard Earth Sciences Data and Information Services Center  
33 (GES DISC), Accessed June 2016, 10.5067/7MCPBJ41Y0K6
- 34 Global Modeling and Assimilation Office (GMAO)(2015f), MERRA-2 tavg1\_2d\_rad\_Nx: 2d,1-  
35 Hourly,Time-Averaged,Single-Level,Assimilation,Radiation Diagnostics V5.12.4,  
36 Greenbelt, MD, USA, Goddard Earth Sciences Data and Information Services Center  
37 (GES DISC), Accessed June 2016, 10.5067/Q9QMY5PBNV1T
- 38 Govekar, P. D., C. Jakob, C., and J. Catto (2014), The relationship between clouds and dynamics  
39 in Southern Hemisphere extratropical cyclones in the real world and a climate model, *J.*  
40 *Geophys. Res. Atmos.*, 119, 6609–6628, doi:10.1002/2013JD020699.

- Grandey, B. S., P. Stier, R. G. Grainger, and T. M. Wagner (2013), The contribution of the strength and structure of extratropical cyclones to observed cloud–aerosol relationships, *Atmos. Chem. Phys.*, 13, 10689–10701, doi:10.5194/acp-13-10689-2013.
- Grant, W. B., et al. (2000), A case study of transport of tropical marine boundary layer and lower tropospheric air masses to the northern midlatitude upper troposphere, *J. Geophys. Res.*, 105(D3), 3757–3769, doi:10.1029/1999JD901022.
- Hegarty, J., H. Mao, and R. Talbot (2010), Winter- and summertime continental influences on tropospheric O<sub>3</sub> and CO observed by TES over the western North Atlantic Ocean, *Atmos. Chem. Phys.*, 10, 3723–3741, doi:10.5194/acp-10-3723-2010.
- Hegglin, M. I. and T. G. Shepherd (2009), Large climate-induced changes in ultraviolet index and stratosphere-to-troposphere ozone flux, *Nature Geosci.*, 2, 687, doi:10.1038/ngeo604.
- Herman, R. L., and S. S. Kulawik (2013), *Tropospheric Emission Spectrometer TES Level 2 (L2) data user's guide*, D-38042, version 5.0, Jet Propulsion Laboratory, California Institute of Technology, Pasadena, CA, available online at <http://tes.jpl.nasa.gov/documents>, 2013.
- Hess, P. G. and R. Zbinden (2013), Stratospheric impact on tropospheric ozone variability and trends: 1990–2009, *Atmos. Chem. Phys.*, 13, 649–674, doi:10.5194/acp-13-649-2013.
- Hoinka, K. P. (1998), Statistics of the global tropopause pressure, *Mon. Weather Rev.*, 126, 12, 3303–3325, 1998.
- Holton, J. R., P. H. Haynes, M. E. McIntyre, A. R. Douglass, R. B. Rood, and L. Pfister (1995), Stratosphere-troposphere exchange, *Rev. Geophys.*, 33, 403–439, doi:10.1029/95RG02097.
- Hoskins, B. J., M. E. McIntyre, and A. W. Robertson (1985), On the use and significance of isentropic potential vorticity maps, *Q. J. R. Meteorol. Soc.*, 111, 877–946.
- Hoskins, B. J., and K. I. Hodges (2002), New perspectives on the northern hemisphere winter storm tracks, *J. Atmos. Sci.*, 59, 1041–1061.
- Hsu, J., M. J. Prather, M. J., and O. Wild (2005), Diagnosing the stratosphere-to-troposphere flux of ozone in a chemistry transport model, *J. Geophys. Res.*, 110, D19305, doi:10.1029/2005JD006045, 2005.
- Hsu, J., and M. J. Prather (2009), Stratospheric variability and tropospheric ozone, *J. Geophys. Res.*, 114, D06102, doi:10.1029/2008JD010942.
- Hudman, R. C., et al. (2004), Ozone production in transpacific Asian pollution plumes and implications for ozone air quality in California, *J. Geophys. Res.*, 109, D23S10, doi:10.1029/2004JD004974.
- Jaffe, D., H. Price, D. Parrish, A. Goldstein, and J. Harris (2003), Increasing background ozone during spring on the west coast of North America, *Geophys. Res. Lett.*, 30(12), 1613, doi:10.1029/2003GL017024.
- James, P., A. Stohl, C. Forster, S. Eckhardt, P. Seibert, and A. Frank (2003), A 15-year climatology of stratosphere-troposphere exchange with a Lagrangian particle dispersion

- 1 model: 2. Mean climate and seasonal variability, *J. Geophys. Res.*, 108(D12), 8522,  
2 doi:10.1029/2002JD002639.
- 3 Jiang, J. H., H. Su, C. Zhai, L. Wu, K. Minschwaner, A. M. Molod, and A. M. Tompkins (2015),  
4 An assessment of upper troposphere and lower stratosphere water vapor in MERRA,  
5 MERRA2, and ECMWF reanalyses using Aura MLS observations, *J. Geophys. Res.*  
6 *Atmos.*, 120, 11,468–11,485, doi:10.1002/2015JD023752.
- 7 Johnson W.B. and Viezee W. (1981), Stratospheric ozone in the lower troposphere-I.  
8 Presentation and interpretation of aircraft measurements, *Atmos. Environ.*, 15, 1309-  
9 1323.
- 10 Kawase, H., T. Nagashima, K. Sudo, and T. Nozawa (2011), Future changes in tropospheric  
11 ozone under Representative Concentration Pathways (RCPs), *Geophys. Res. Lett.*, 38,  
12 L05801, doi:10.1029/2010GL046402.
- 13 Klein, S. A., and C. Jakob (1999), Validation and sensitivities of frontal clouds simulated by the  
14 ECMWF model, *Mon. Wea. Rev.*, 127, 2514–2531.
- 15 Knowland, K. E., R. M. Doherty, and K. I. Hodges (2015), The effects of springtime mid-  
16 latitude storms on trace gas composition determined from the MACC reanalysis, *Atmos.*  
17 *Chem. Phys.*, 15, 3605-3628, doi:10.5194/acp-15-3605-2015.
- 18 Knowland, K. E., Ott, L. E., Duncan, B. N., & Wargan, K. (2017), Stratospheric intrusion-  
19 influenced ozone air quality exceedances investigated in the NASA MERRA-2  
20 reanalysis, *Geophys. Res. Lett.*, 44, doi: 10.1002/2017GL074532.
- 21 Kuang, S., M. J. Newchurch, J. Burris, L. Wang, K. Knupp, and G. Huang (2012), Stratosphere-  
22 to-troposphere transport revealed by ground-based lidar and ozonesonde at a midlatitude  
23 site, *J. Geophys. Res.*, 117, D18305, doi:10.1029/2012JD017695.
- 24 Lamarque, J.-F. and P. G. Hess (1994), Cross-tropopause mass exchange and potential vorticity  
25 budget in a simulated tropopause folding, *J. Atmos. Sci.*, 51, 2246–2246,  
26 doi:10.1175/1520-0469.
- 27 Langford, A. O., and S. J. Reid (1998), Dissipation and mixing of a small-scale stratospheric  
28 intrusion in the upper troposphere, *J. Geophys. Res.*, 103, D23, 31,265-31,276, doi:  
29 10.1029/98JD02596.
- 30 Langford, A. O., K. C. Aikin, C. S. Eubank, and E. J. Williams (2009), Stratospheric  
31 contribution to high surface ozone in Colorado during springtime, *Geophys. Res. Lett.*,  
32 36, L12801, doi: 10.1029/2009GL038367.
- 33 Lau, N. C., and M. W. Crane (1995), A satellite view of the synoptic- scale organization of cloud  
34 properties in midlatitude and tropical circulation systems, *Mon. Wea. Rev.*, 123, 1984–  
35 2006.
- 36 Lefohn, A. S., H. Wernli, D. Shadwick, S. Limbach, S. J. Oltmans, and M. Shapiro (2011), The  
37 importance of stratospheric-tropospheric transport in affecting surface ozone  
38 concentrations in the western and northern tier of the United States, *Atmos. Environ.*, 45,  
39 4845–4857, doi:10.1016/j.atmosenv.2011.06.014.
- 40 Liang, Q., et al. (2007), Summertime influence of Asian pollution in the free troposphere over  
41 North America, *J. Geophys. Res.*, 112, D12S11, diu: 10.1029/2006JD007919.

- 1 Lin, M., A. M. Fiore, O. R. Cooper, L. W. Horowitz, A. O. Langford, H. Levy II, B. J. Johnson,  
2 V. Naik, S. J. Oltmans, and C. J. Senff (2012), Springtime high surface ozone events over  
3 the western United States: Quantifying the role of stratospheric intrusions, *J. Geophys.*  
4 *Res.*, 117, D00V22, doi:10.1029/2012JD018151.
- 5 Lin, M. Y., A. M. Fiore, L.W. Horowitz, A. O. Langford, S. J. Oltmans, D. Tarasick, and H. E.  
6 Rieder (2015), Climate variability modulates western U.S. ozone air quality in spring via  
7 deep stratospheric intrusions, *Nat. Commun.*, 6, 7105, doi:10.1038/ncomms8105.
- 8 Liu, H., D. J. Jacob, L. Y. Chan, S. J. Oltmans, I. Bey, R. M. Yantosca, J. M. Harris, B. N.  
9 Duncan, and R. V. Martin (2002), Sources of tropospheric ozone along the Asian Pacific  
10 Rim: An analysis of ozonesonde observations, *J. Geophys. Res.*, 107(D21), 4573,  
11 doi:10.1029/2001JD002005.
- 12 Livesey, N.J., W. G. Read, P. A. Wagner, L. Froidevaux, A. Lambert, G. L. Manney, L. F.  
13 Millan Valle, H. C. Pumphrey, M. L. Santee, M. J. Schwartz, S. Wang, R. A. Fuller, R. F.  
14 Jarnot, B. W. Knosp and E. Martinez (2017), Version 4.2x Level 2 data quality and  
15 description document, *JPL D-33509 Rev. C*.
- 16 Logan, J. A. (1999), An analysis of ozonesonde data for the lower stratosphere:  
17 Recommendations for testing models, *J. Geophys. Res.*, 104(D13), 16151–16170,  
18 doi:10.1029/1999JD900216.
- 19 Logan, J. A., et al. (2012), Changes in ozone over Europe: Analysis of ozone measurements from  
20 sondes, regular aircraft (MOZAIC) and alpine surface sites, *J. Geophys. Res.-Atmos.*,  
21 117, D09301, doi:10.1029/2011jd016952.
- 22 Manney, G. L., R. S. Harwood, I. A. MacKenzie, K. Minschwaner, D. R. Allen, M. L. Santee, K.  
23 A. Walker, M. I. Hegglin, A. Lambert, H. C. Pumphrey, P. F. Bernath, C. D. Boone, M.  
24 J. Schwartz, N. J. Livesey, W. H. Daffer, R. A. Fuller (2009), Satellite observations and  
25 modeling of transport in the upper troposphere through the lower mesosphere during the  
26 2006 major stratospheric sudden warming, *Atmos. Chem. Phys.*, 9, 4775–4795,  
27 doi:10.5194/acp-9-4775-2009.
- 28 Manney, G. L., M. I. Hegglin, D. H. Daffer, M. L. Santee, E. A. Ray, S. Pawson, M. J.  
29 Schwartz, C. D. Boone, L. Froidevaux, N. J. Livesey, W. G. Read, and K. A. Walker  
30 (2011), Jet characterization in the upper troposphere/lower stratosphere (UTLS):  
31 applications to climatology and transport studies, *Atmos. Chem. Phys.*, 11, 6115–6137,  
32 doi: 10.5194/acp-11-6115-2011.
- 33 Manobianco, J. (1989), Explosive east coast cyclogenesis over the west-central North Atlantic  
34 Ocean: A composite study derived from ECMWF operational analyses, *Mon. Wea. Rev.*,  
35 117, 2365–2383.
- 36 Mari, C., D. J. Jacob, and P. Bechtold (2000), Transport and scavenging of soluble gases in a  
37 deep convective cloud, *J. Geophys. Res.*, 105(D17), 22255–22267,  
38 doi:10.1029/2000JD900211.
- 39 McCarty, W., L. Coy, R. Gelaro, A. Huang, D. Merkova, E. B. Smith, M. Sienkiewicz, and K.  
40 Wargan (2016), MERRA-2 input observations: Summary and initial assessment.  
41 Technical Report Series on Global Modeling and Data Assimilation, Vol. 46, NASA

- 1 Tech. Rep. NASA/TM–2016–104606, 61 pp. [Available online at  
2 <https://gmao.gsfc.nasa.gov/pubs/docs/McCarty885.pdf>.]
- 3 McLinden, C. A., S. C. Olsen, B. Hannegan, O. Wild, M. J. Prather, and J. Sundet (2000),  
4 Stratospheric ozone in 3-D models: A simple chemistry and the cross-tropopause flux, *J.*  
5 *Geophys. Res.*, 105, 14,653–14,665, doi:10.1029/2000JD900124.
- 6 Meloen, J., et al. (2003), Stratosphere-troposphere exchange: A model and method  
7 intercomparison, *J. Geophys. Res.*, 108, 8526, doi:10.1029/2002JD002274.
- 8 Miyazaki, Y., et al. (2003), Synoptic-scale transport of reactive nitrogen over the western Pacific  
9 in spring, *J. Geophys. Res.*, 108(D20), 8788, doi:10.1029/2002JD003248.
- 10 Molod, A., L. Takacs, M. Suarez, and J. Bacmeister (2015), Development of the GEOS-5  
11 atmospheric general circulation model: Evolution from MERRA to MERRA2, *Geosci.*  
12 *Model Dev.*, 8, 1339–1356, doi:10.5194/gmd-8-1339-2015.
- 13 Monks, P. S. (2000), A review of the observations and origins of the spring ozone maximum,  
14 *Atmos. Environ.*, 34, 3545–3561.
- 15 Moody, J., J. Davenport, J. Merrill, S. Oltmans, D. Parrish, J. Holloway, H. Levy II, G. Forbes,  
16 M. Trainer, and M. Buhr (1996), Meteorological mechanisms for transporting O<sub>3</sub> over  
17 the western North Atlantic Ocean: A case study for August 24–29, 1993, *J. Geophys.*  
18 *Res.*, 101(D22), 29213–29227, doi: 10.1029/96JD00885.
- 19 Naud, C. M., D. J. Posselt, and S. C. van den Heever (2012), Observational analysis of cloud and  
20 precipitation in midlatitude cyclones: Northern versus southern hemisphere warm fronts,  
21 *J. Climate*, 25, 5135–5151, doi:10.1175/JCLI-D-11-00569.1.
- 22 Naud, C. M., J. F. Booth, A. D. Del Genio (2014), Evaluation of ERA-Interim and MERRA  
23 Cloudiness in the Southern Ocean, *J. Climate*, 27, 5, 2109–2124, doi:10.1175/JCLI-D-13-  
24 00432.1.
- 25 Neu, J. L., T. Flury, G. L. Manney, M. K. Santee, N. J. Livesey, and J. Worden (2014),  
26 Tropospheric ozone variations governed by changes in stratospheric circulation, *Nat.*  
27 *Geosci.*, 7, 340–344, doi: doi:10.1038/ngeo2138.
- 28 Olsen, M. and J. Stanford, J. (2001), Evidence of stratosphere-to-troposphere transport within a  
29 mesoscale model and Total Ozone Mapping Spectrometer total ozone, *J. Geophys. Res.*,  
30 106, 27323–27334, doi: 10.1029/2001JD900202.
- 31 Olsen, M. A., M. R. Schoeberl, and A. R. Douglass (2004), Stratosphere-troposphere exchange  
32 of mass and ozone, *J. Geophys. Res.*, 109, D24114, doi:10.1029/2004JD005186.
- 33 Olsen, M. A., A. R. Douglass, and T. B. Kaplan (2013), Variability of extratropical ozone  
34 stratosphere–troposphere exchange using microwave limb sounder observations, *J.*  
35 *Geophys. Res. Atmos.*, 118, 1090–1099, doi:10.1029/2012JD018465.
- 36
- 37 Orbe, C., D. W. Waugh, H. Yang, J.-F. Lamarque, S. Tilmes, and D. E. Kinnison (2017),  
38 Tropospheric transport differences between models using the same large-scale  
39 meteorological fields, *Geophys. Res. Lett.*, 44, 1068–1078, doi:10.1002/2016GL071339.

- 1 Ott, L. E., et al. (2016), Frequency and impact of summertime stratospheric intrusions over  
2 Maryland during DISCOVER-AQ (2011): New evidence from NASA's GEOS-5  
3 simulations, *J. Geophys. Res. Atmos.*, 121, 3687–3706, doi:10.1002/2015JD024052.
- 4 Parrish, D. D., K. S. Law, J. Staehelin, R. Derwent, O. R. Cooper, H. Tanimoto, A. Volz-  
5 Thomas, S. Gilge, H.-E. Scheel, M. Steinbacher, and E. Chan (2012), Long-term changes  
6 in lower tropospheric baseline ozone concentrations at northern mid-latitudes, *Atmos.*  
7 *Chem. Phys.*, 12, 11485-11504, doi:10.5194/acp-12-11485-2012.
- 8 Patoux, J., X. Yuan and C. Li (2009), Satellite-based midlatitude cyclone statistics over the  
9 Southern Ocean. Part I: Scatterometer-derived pressure fields and storm tracking, *Journal*  
10 *of Geophysical Research*, D04105, doi:10.1029/2008JD010873.
- 11 Pavelin, E., and J. A. Whiteway (2002), Gravity wave interactions around the jet stream,  
12 *Geophys. Res. Lett.*, 29(21), 2024, doi:10.1029/2002GL015783.
- 13 Pawson, S., I. Stajner, S. R. Kawa, H. Hayashi, W.-W. Tan, J. E. Nielsen, Z. Zhu, L.-P. Chang,  
14 and N. J. Livesey (2007), Stratospheric transport using 6-h-averaged winds from a data  
15 assimilation system, *J. Geophys. Res.*, 112, D23103, doi:10.1029/2006JD007673.
- 16 Polvani, L. M., and J. G. Esler (2007), Transport and mixing of chemical air masses in idealized  
17 baroclinic life cycles, *J. Geophys. Res.*, 112, D23102, doi:10.1029/2007JD008555.
- 18 Raveh-Rubin, S. (2017), Dry Intrusions: Lagrangian Climatology and Dynamical Impact on the  
19 Planetary Boundary Layer, *J. Climate*, 30, 6661–6682, doi: 10.1175/JCLI-D-16- [0782.1](#)
- 20 Reed, R. J., and F. Sanders (1953), An investigation of the development of a mid-tropospheric  
21 frontal zone and its associated vorticity field, *J. Meteorol.*, 10, 338-349.
- 22 Reutter, P., B. Škerlak, M. Sprenger, and H. Wernli (2015), Stratosphere–troposphere exchange  
23 (STE) in the vicinity of North Atlantic cyclones, *Atmos. Chem. Phys.*, 15, 10939-10953,  
24 doi:10.5194/acp-15-10939-2015.
- 25 Rienecker, M. M., et al. (2011), MERRA: NASA's Modern-Era Retrospective Analysis for  
26 Research and Applications, *J. Clim.*, 24, 3624–3648, doi:10.1175/JCLI-D-11-00015.1.
- 27 Rood, R. B., A. R. Douglass, M. C. Cerniglia, and W. G. Read (1997), Synoptic scale mass  
28 exchange from the troposphere to the stratosphere, *J. Geophys. Res.*, 102, 23,467–  
29 23,486, doi: 10.1029/97JD01598.
- 30 Schoeberl, M. R., A. R. Douglass, Z. Zhu, and S. Pawson (2003), A comparison of the lower  
31 stratospheric age-spectra derived from a general circulation model and two data  
32 assimilation systems, *J. Geophys. Res.*, 108(D3), 4113, doi:10.1029/2002JD002652.
- 33 Schoeberl, M. R. (2004), Extratropical stratosphere-troposphere mass exchange, *J. Geophys.*  
34 *Res.*, 109, D13303, doi:10.1029/2004JD004525.
- 35 Shapiro, M. A. (1980), Turbulent mixing within tropopause folds as a mechanism for the  
36 exchange of chemical constituents between the stratosphere and troposphere, *J. Atmos.*  
37 *Sci.*, 37, 994– 1004.
- 38 Shaw, T. A., M. Baldwin, E. A. Barnes, R. Caballero, C. I. Garfinkel, Y.-T. Hwang, C. Li, P. A.  
39 O’Gorman, G. Rivière, I. R. Simpson and A. Voigt (2016), Storm track processes and the

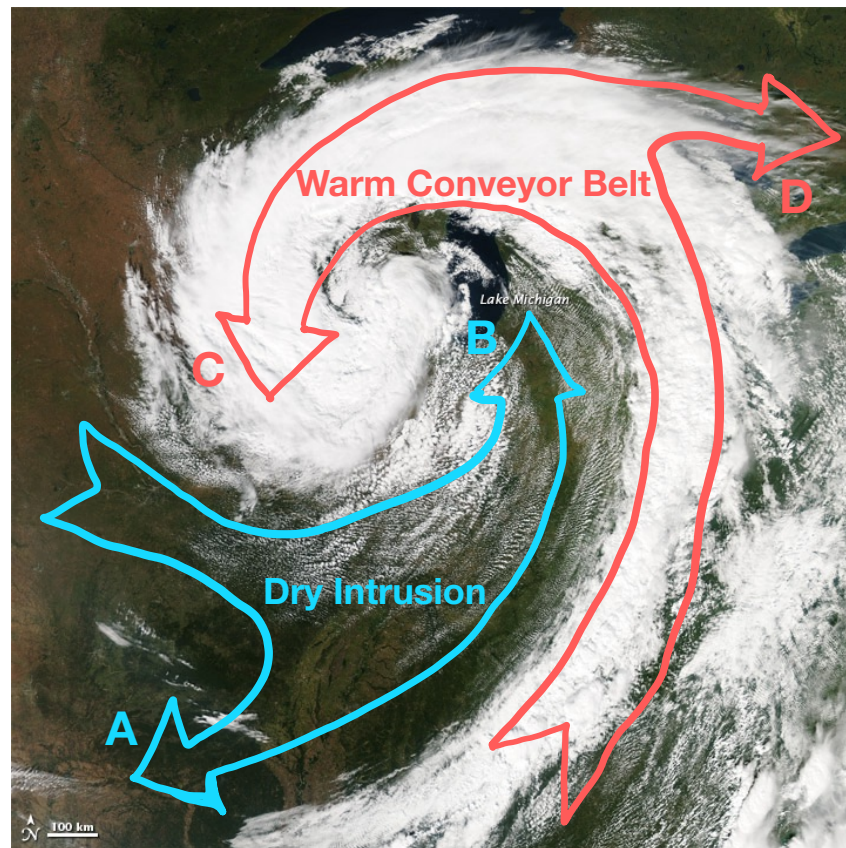


- opposing influences of climate change, *Nat. Geosci.*, 9, 656–664, doi:  
10.1038/NCEO2783
- Sinclair, M. R., (1997), Objective identification of cyclones and their circulation intensity, and climatology, *Wea. Forecasting*, 12, 591–608.
- Sinclair, M. R. (1995), A climatology of cyclogenesis for the Southern Hemisphere, *Mon. Wea. Rev.*, 123, 1601–1619, 1995.
- Škerlak, B., M. Sprenger, and H. Wernli (2014), A global climatology of stratosphere-troposphere exchange using the ERA-Interim data set from 1979 to 2011, *Atmos. Chem. Phys.*, 14, 913–937, doi:10.5194/acp-14-913-2014.
- Škerlak, B., M. Sprenger, S. Pfahl, E. Tyrlis, and H. Wernli (2015), Tropopause folds in ERA-Interim: Global climatology and relation to extreme weather events, *J. Geophys. Res. Atmos.*, 120, 4860–4877, doi:10.1002/2014JD022787.
- Simpson, I. R., T. A. Shaw, and R. Seager (2014), A diagnosis of the seasonally and longitudinally varying mid-latitude circulation response to global warming, *J. Atmos. Sci.*, 71, 2489–2515, doi: 10.1175/JAS-D-13-0325.1
- Spaete, P., D. R. Johnson, and T. K. Schaack (1994), Stratospheric tropospheric mass exchange during the Presidents’ Day Storm, *Mon. Weather Rev.*, 122, 424–439.
- Sprenger, M., and H. Wernli (2003), A northern hemispheric climatology of cross-tropopause exchange for the ERA15 time period (1979 – 1993), *J. Geophys. Res.*, 108(D12), 8521, doi:10.1029/2002JD002636.
- Stajner, I., et al. (2008), Assimilated ozone from EOS-Aura: Evaluation of the tropopause region and tropospheric columns, *J. Geophys. Res.*, 113, D16S32, doi:10.1029/2007JD008863.
- Stevenson, D. S., et al. (2006), Multimodel ensemble simulations of present-day and near-future tropospheric ozone, *J. Geophys. Res.*, 111, D08301, doi:10.1029/2005JD006338.
- Stohl, A., et al. (2003), Stratosphere-troposphere exchange: A review, and what we have learned from STACCATO, *J. Geophys. Res.*, 108(D12), 8516, doi:10.1029/2002JD002490.
- Stohl, A., O. R. Cooper, and P. James (2004), A cautionary note on the use of meteorological analysis fields for quantifying atmospheric mixing, *J. Atmos. Sci.*, 61 (12), 1446–1453, doi:10.1175/1520-0469(2004)061<1446:ACNOTU>2.0.CO;2
- Strode, S. A., J. M. Rodriguez, J. A. Logan, O. R. Cooper, J. C. Witte, L. N. Lamsal, M. Damon, B. Van Aartsen, S. D. Steenrod, and S. E. Strahan (2015), Trends and variability in surface ozone over the United States, *J. Geophys. Res.-Atmos.*, 120, 9020–9042, doi:10.1002/2014JD022784.
- Sudo, K., M. Takahashi, and H. Akimoto (2003), Future changes in stratosphere-troposphere exchange and their impacts on future tropospheric ozone simulations, *Geophys. Res. Lett.*, 30, 2256, doi:10.1029/2003GL018526.
- Sullivan, J. T., T. J. McGee, A. M. Thompson, R. B. Pierce, G. K. Sumnicht, L. W. Twigg, E. Eloranta, and R. M. Hoff (2015), Characterizing the lifetime and occurrence of stratospheric-tropospheric exchange events in the rocky mountain region using high-

- 1 resolution ozone measurements, *J. Geophys. Res.-Atmos.*, 120, 12,410–12,424,  
2 doi:10.1002/2015JD023877.
- 3 Tan, W. W., M. A. Geller, S. Pawson, and A. da Silva (2004), A case study of excessive  
4 subtropical transport in the stratosphere of a data assimilation system, *J. Geophys. Res.*,  
5 109, D11102, doi:10.1029/2003JD004057.
- 6 Tang, Q. and M. J. Prather (2012), Five blind men and the elephant: what can the NASA Aura  
7 ozone measurements tell us about stratosphere-troposphere exchange?, *Atmos. Chem.*  
8 *Phys.*, 12, 2357–2380, doi:10.5194/acp-12-2357-2012.
- 9 Thorncroft, C. D., B. J. Hoskins, and M. E. McIntyre (1993), Two paradigms of baroclinic wave  
10 life-cycle behaviour, *Q. J. R. Meteorol. Soc.*, 119, 17–55.
- 11 Tian, B., E. J. Fetzer, B. H. Kahn, J. Teixeira, E. Manning, and T. Hearty (2013), Evaluating  
12 CMIP5 Models using AIRS Tropospheric Air Temperature and Specific Humidity  
13 Climatology, *J. Geophys. Res.-Atmos.*, 118, 114–134, doi:10.1029/2012JD018607.
- 14 Ulbrich, U., G. C. Leckebusch, and J. G. Pinto (2009), Extratropical cyclones in the present and  
15 future climate: a review, *Theor. Appl. Climatol.*, 96, 117, doi:10.1007/s00704-008-0083-  
16 8.
- 17 Verstraeten, W. W., K. F. Boersma, J. Zorner, M. A. F. Allaart, K. W. Bowman, and J. R.  
18 Worden (2013), Validation of six years of TES tropospheric ozone retrievals with  
19 ozonesonde measurements: implications for spatial patterns and temporal stability in the  
20 bias, *Atmos. Meas. Techn.*, 6, 1413–1423, 2013, doi:10.5194/amt-6-1413-2013.
- 21 Verstraeten, W. W., J. L. Neu, J. E. Williams, K. W. Bowman, J. R. Worden, K. F. Boersma  
22 (2015), Rapid increases in tropospheric ozone production and export from China  
23 published, *Nature Geosci.*, 2015, 8, 690–695, doi:10.1038/ngeo2493.
- 24 Wallace, J. M. and P. V. Hobbs (2006), Atmospheric Science – An introductory survey, 2<sup>nd</sup>  
25 edition, Academic Press.
- 26 Waters, J. W., et al. (2006), The Earth Observing System Microwave Limb Sounder (EOS MLS)  
27 on the Aura satellite, *IEEE T. Geosci. Remote*, 44, 1075–1092,  
28 doi:10.1109/TGRS.2006.873771.
- 29 Wang, Y., D. J. Jacob, and J. A. Logan (1998), Global simulation of tropospheric O<sub>3</sub>-NO<sub>x</sub>-  
30 hydrocarbon chemistry, 3. Origin of tropospheric ozone and effects of non-methane  
31 hydrocarbons, *J. Geophys. Res.*, 103, 10,757–10,768.
- 32 Wang, X. L., V. R. Swail, and F. W. Zwiers (2006), Climatology and changes of extratropical  
33 cyclone activity: Comparison of ERA-40 with NCEP/NCAR reanalysis for 1958–2001, *J.*  
34 *Climate*, 19, 3145–3166.
- 35 Wargan, K., S. Pawson, M. A. Olsen, J. C. Witte, A. R. Douglass, J. R. Ziemke, S. E. Strahan,  
36 and J. E. Nielsen (2015), The global structure of upper troposphere-lower stratosphere  
37 ozone in GEOS-5: A multiyear assimilation of EOS Aura data, *J. Geophys. Res.-Atmos.*,  
38 120, 2013–2036, doi:10.1002/2014JD022493.
- 39 Wargan, K., G. Labow, S. Frith, S. Pawson, N. Livesey, and G. Partyka (2017), Evaluation of the  
40 Ozone Fields in NASA’s MERRA-2 Reanalysis, *J. Climate*, 30, 2961–2988,  
41 <https://doi.org/10.1175/JCLI-D-16-0699.1>

- 1 Wernli, H. and H. Davies (1997), A Lagrangian-based analysis of extratropical cyclones. 1: The  
2 method and some applications, *Q. J. Roy. Meteor. Soc.*, 123, 467–489.
- 3 Wernli, H., and M. Bourqui (2002), A Lagrangian “1-year climatology” of (deep) cross-  
4 tropopause exchange in the extratropical northern hemisphere, *J. Geophys. Res.*, 107(D2),  
5 4021, doi:10.1029/2001JD000812.
- 6 Wernli, H., and C. Schwiertz (2006), Surface cyclones in the ERA-40 dataset (1958-2001). Part I:  
7 Novel identification method and global climatology, *J. Atmos. Sci.*, 63, 2486–2507.
- 8 Whitaker, J., L.W. Uccellini, and K. F. Brill (1988), A model-based diagnostic study of the rapid  
9 development phase of the Presidents’ Day cyclone, *Mon. Wea. Rev.*, 116, 2337–2365.
- 10 Wild, O. (2007), Modelling the global tropospheric ozone budget: exploring the variability in  
11 current models, *Atmos. Chem. Phys.*, 7, 2643–2660, doi:10.5194/acp-7-2643-2007.
- 12 Wirth, V. and J. Egger (1999), Diagnosing extratropical synoptic-scale stratosphere–troposphere  
13 exchange: a case study, *Q. J. Roy. Meteor. Soc.*, 125, 635–655,  
14 doi:10.1002/qj.49712555413.
- 15 Wu, S. L., L. J. Mickley, D. J., Jacob, J., Logan, R. M., Yantosca, and D. Rind (2007), Why are  
16 there large differences between models in global budgets of tropospheric ozone?, *J.*  
17 *Geophys. Res.-Atmos.*, 112, D05302, doi:10.1029/2006jd007801.
- 18 Young, P. J., et al. (2013), Pre-industrial to end 21st century projections of tropospheric ozone  
19 from the Atmospheric Chemistry and Climate Model Intercomparison Project  
20 (ACCMIP), *Atmos. Chem. Phys.*, 13, 2063-2090, doi:10.5194/acp-13-2063-2013, 2013.
- 21 Zappa, G., L. C. Shaffrey, K. I. Hodges, P.G. Sansom, and D. B. Stephenson (2013), A  
22 multimodel assessment of future projections of the North Atlantic and European  
23 extratropical cyclones in the CMIP5 climate models, *J. Clim.*, 26, 5846–5862, doi:  
24 <https://doi.org/10.1175/JCLI-D-12-00573.1>
- 25 Zheng, G. and J. A. Pyle (2005), Influence of El Niño Southern Oscillation on  
26 stratosphere/troposphere exchange and the global ozone budget, *Geophys. Res. Lett.*, 32,  
27 L01814, doi: 10.1029/2004GL021353.
- 28

1  
2  
3



4  
5  
6  
7  
8  
9  
10  
11  
12  
13  
14  
15

**Figure 1.** Mature extratropical cyclone observed on September 26, 2011 by the Moderate Resolution Imaging Spectroradiometer (MODIS) on the Aqua satellite (<http://earthobservatory.nasa.gov/NaturalHazards/view.php?id=52297>). The center of the cyclone is over Lake Michigan in the United States. The blue and red arrows represent flow along sloping isentropic surfaces: branches A and B correspond to the descending dry intrusion, while branches C and D are for the ascending Warm Conveyor Belt.

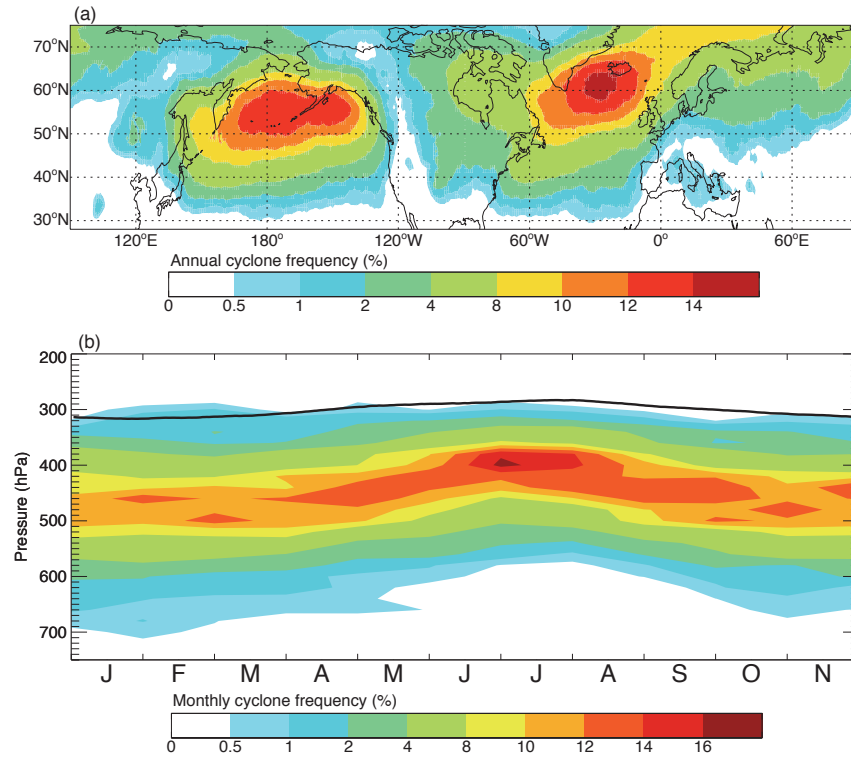


**Figure 2.** (a) Annual mean extratropical cyclone occurrence frequency (%) in the northern hemisphere for 2005-2012. b) Two-dimensional monthly histogram of cyclone tropopause pressure within the dry intrusion. The colors correspond to the percentage of time in a month that extratropical cyclone tropopause pressures are in a given 20 hPa vertical bin. The black line shows to the climatological dynamical tropopause pressure in the northern hemisphere.

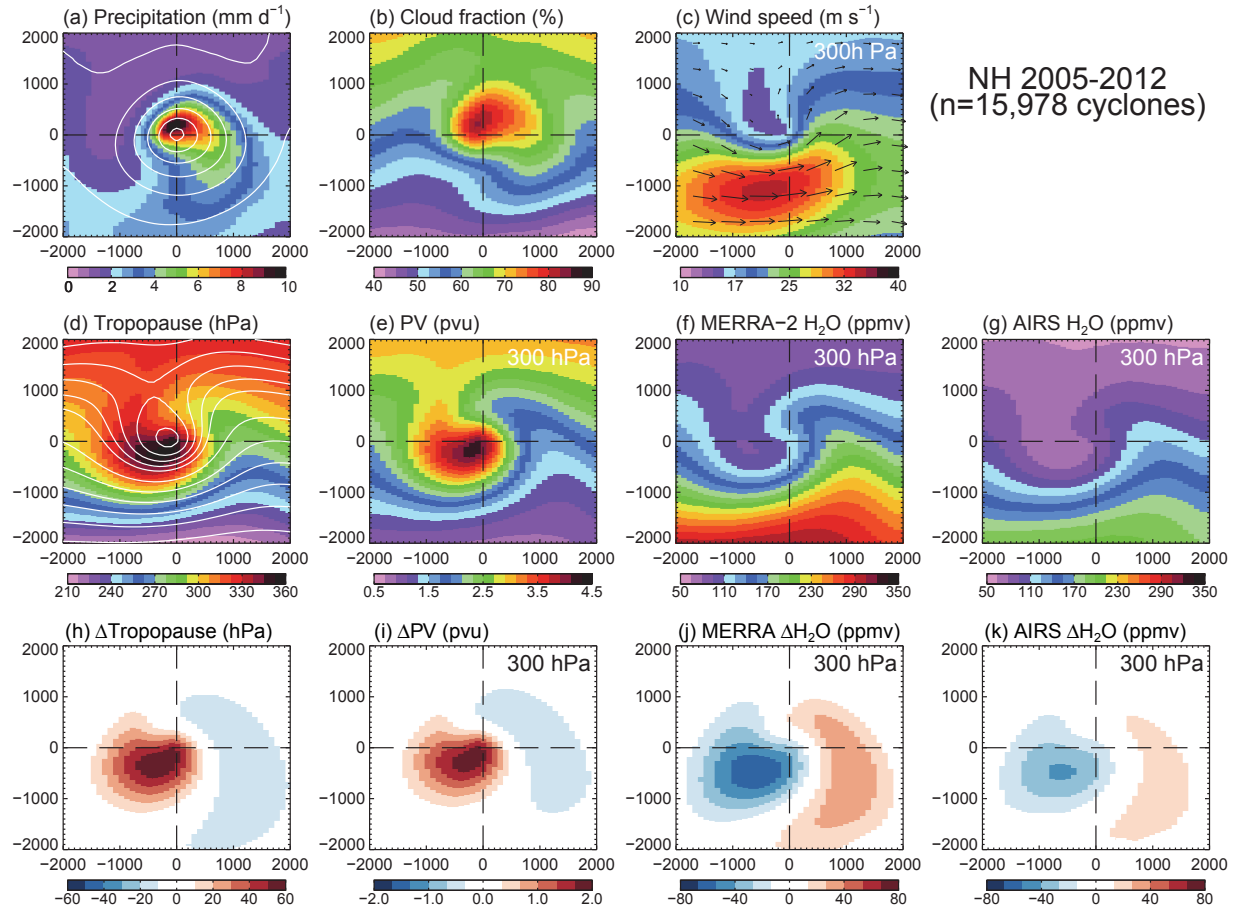


**Figure 3.** MERRA-2 reanalysis composites of 15,978 extratropical cyclones for 2005-2012: (a) Precipitation ( $\text{mm d}^{-1}$ ), with sea level pressure contours in white, (b) total cloud fraction (%), (c) 300 hPa wind speed ( $\text{m s}^{-1}$ ) with arrows indicating vector winds, (d) dynamical tropopause pressure (hPa), with 500hPa geopotential height contours in white, (e) 300 hPa potential vorticity (PV) in pvu, (f) 300 hPa water vapor (ppmv), (g) 300 hPa AIRS water vapor (ppmv), (h) Tropopause anomaly, (i) 300 hPa PV anomaly, (j) 300 hPa water vapor anomaly, (k) AIRS 300 hPa water vapor anomaly. For each of these panels, the numbers along the x and y axes correspond to distance from the cyclone center ( $x = 0$  and  $y = 0$ ) in km, with x increasing in the eastward direction (from -2000 km to +2000km) and y increasing in the poleward direction (from -2000 km to -2000km).

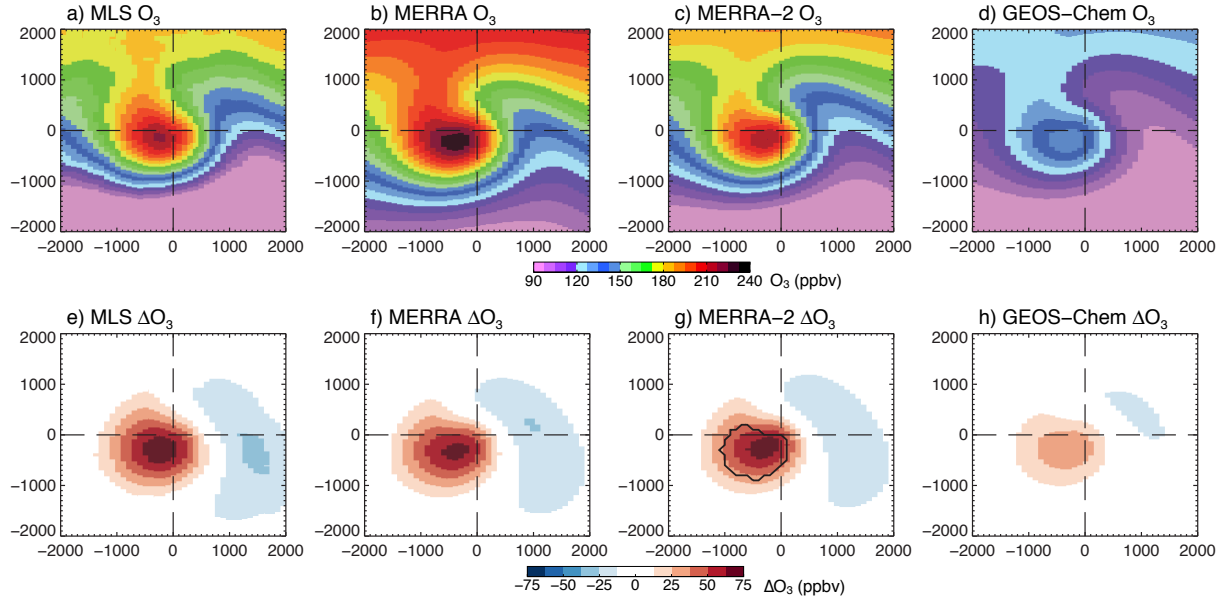


**Figure 4.** Composites of 261 hPa  $O_3$  mixing ratios (ppbv, top panels) and their anomalies  $\Delta O_3$  (ppbv, bottom panels) for MLS (a, e), MERRA (b, f), MERRA-2 (c, g), and GEOS-Chem (d, h). The black contour in Figure 4g shows the area of the dry intrusion as defined in Section 4.1. These composites are for the same cyclones as in Figure 2 and 3.

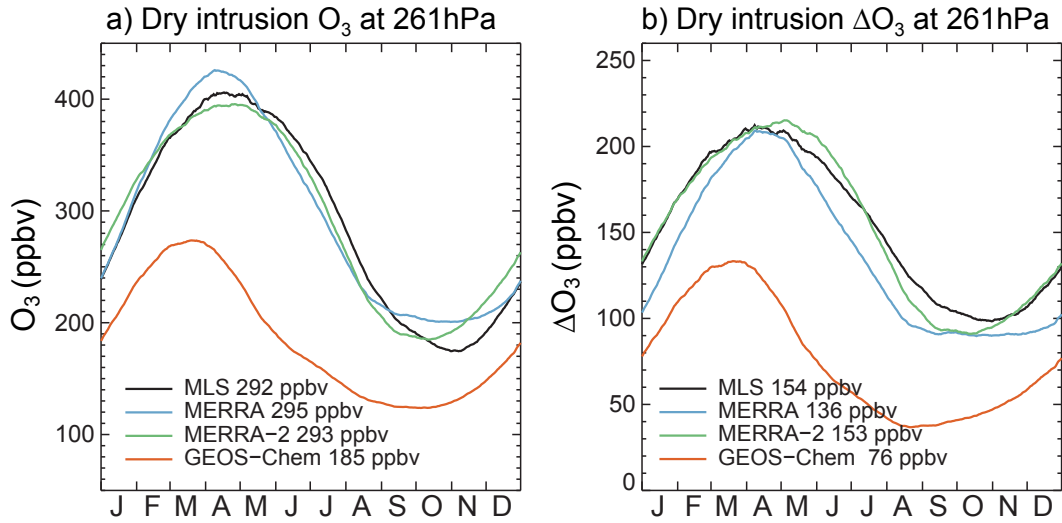


**Figure 5.** (a) Seasonal cycle of 261 hPa  $O_3$  in the dry intrusion of individual cyclones (see text). (b) Dry intrusion  $O_3$  anomalies at 261 hPa. Dry intrusion  $O_3$  and  $\Delta O_3$  are shown for MLS (black line), MERRA (blue line), MERRA-2 (green line), GEOS-Chem (red line). A 40-day boxcar smoothing has been applied to the timeseries.

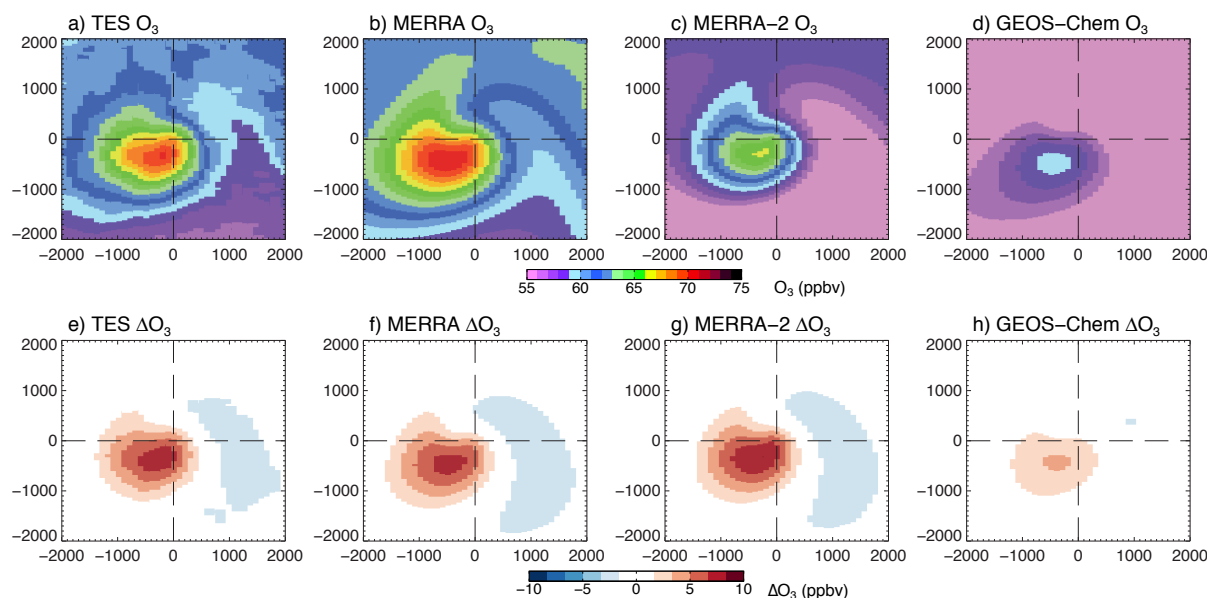


**Figure 6.** Composites of 464 hPa  $O_3$  mixing ratios (top panels) and their anomalies (bottom panels) for TES (a, e), MERRA (b, f), MERRA-2 (c, g), and GEOS-Chem (d, h). The TES averaging kernels and apriori have been applied to the MERRA, MERRA-2, and GEOS-Chem vertical profiles.

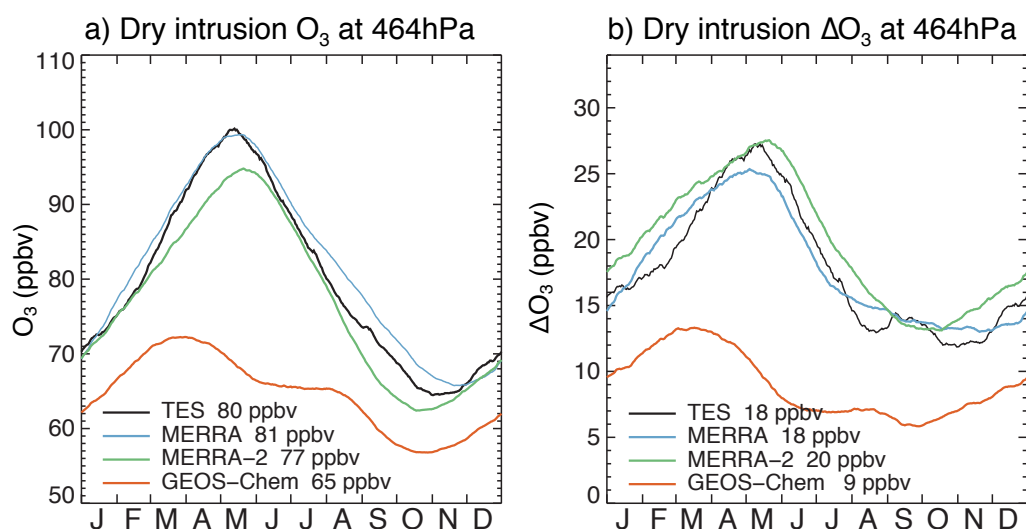


**Figure 7.** (a) Seasonal cycle of 464 hPa  $O_3$  within the dry intrusion of individual cyclones (see text). A 40-day boxcar smoothing has been applied to the timeseries. (b) Dry intrusion  $O_3$  anomalies at 464 hPa. Dry intrusion  $O_3$  and  $\Delta O_3$  are shown for TES (black line), MERRA (blue line), MERRA-2 (green line), GEOS-Chem (red line). The TES averaging kernel and apriori has been applied to the MERRA, MERRA-2, and GEOS-Chem vertical profiles.



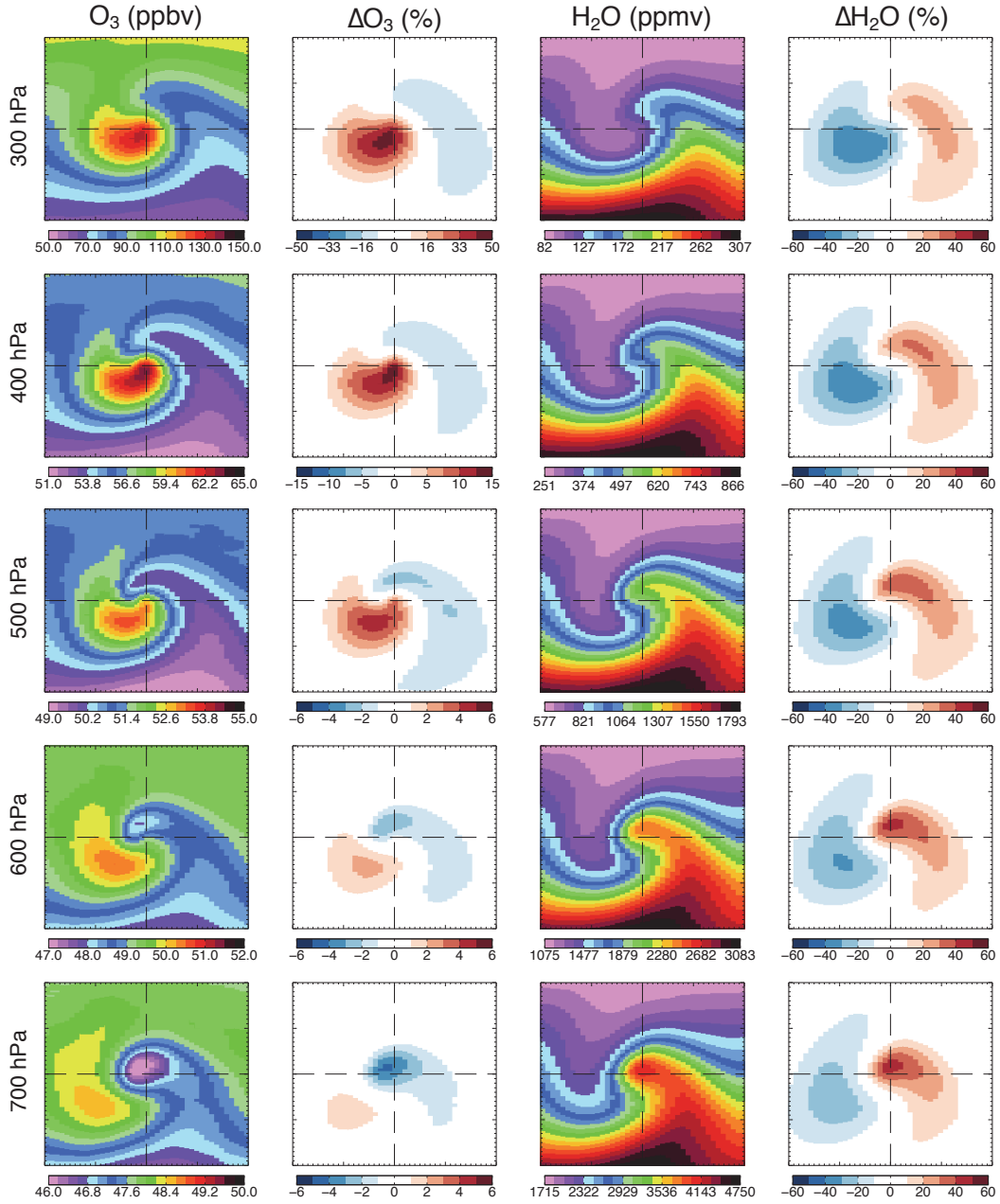


**Figure 8.** MERRA-2 annual composites of O<sub>3</sub> (ppbv, first column) and ΔO<sub>3</sub> (% , second column) for NH extratropical cyclones (2005-2012) at 300, 400, 500, 600, and 700 hPa (rows). The third and fourth column correspond to MERRA-2 composites of H<sub>2</sub>O (ppmv) and ΔH<sub>2</sub>O (%).

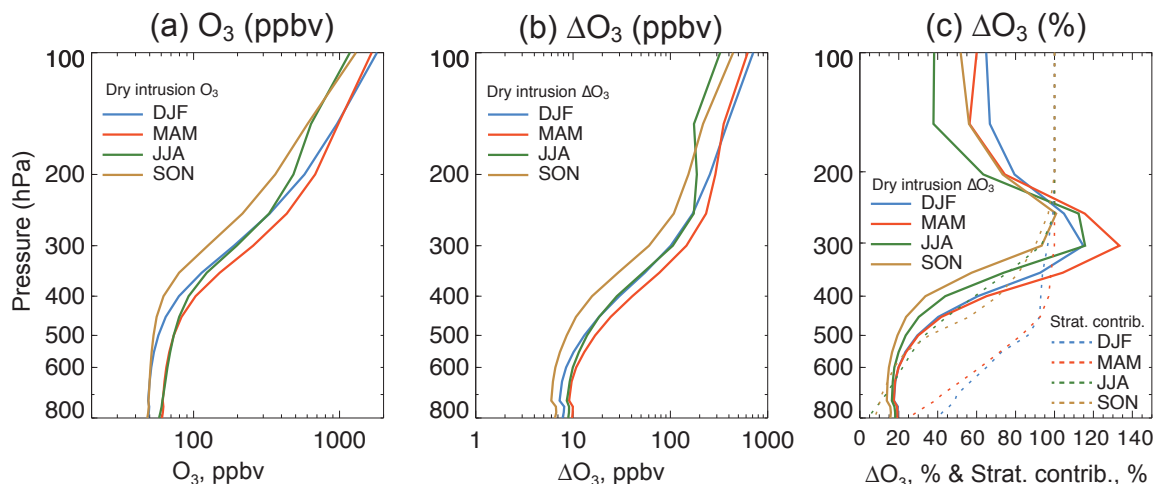


**Figure 9.** Vertical mean profiles of MERRA-2  $O_3$  in the dry intrusions of extratropical cyclones. Absolute ozone values (left panels),  $O_3$  enhancements relative to background ( $\Delta O_3$ , in ppbv: central panels), and percentage enhancements relative to background ( $\Delta O_3$ , in %: right panels). The dashed lines in panel (c) correspond to the fraction of the enhancement that is stratospheric based on the bias-corrected GEOS-Chem tagged simulation.

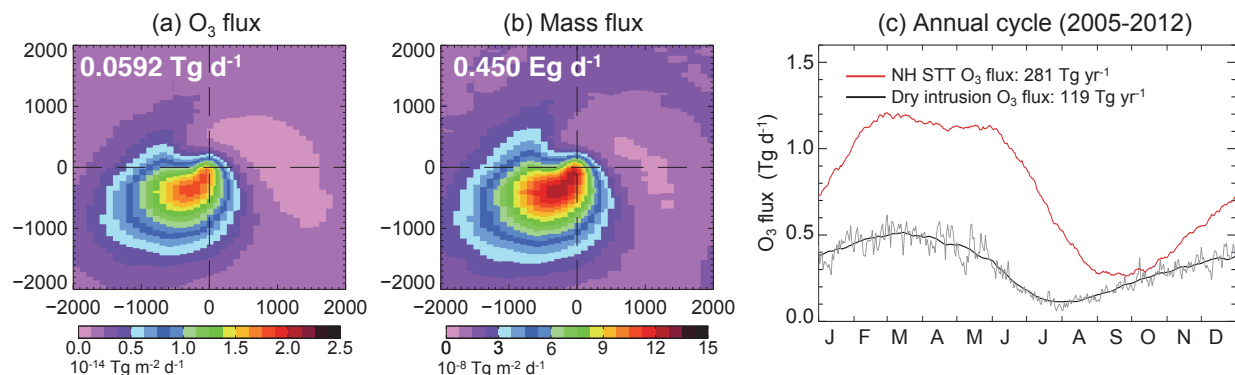


**Figure 10.** Dry intrusion stratosphere-to-troposphere transport (STT) flux of  $O_3$  and mass inferred from MERRA-2 for 2005-2012. Annual mean cyclone-centric composites of STT (a)  $O_3$  flux (units of  $10^{-14}$  Tg  $O_3$   $m^{-2}$   $d^{-1}$ ) and (b) mass flux ( $10^{-8}$  Tg  $m^{-2}$   $d^{-1}$ ). The annual-mean daily composite fluxes are indicated in each panel. (c) Annual cycle of dry intrusion STT  $O_3$  fluxes for NH extratropical cyclones (daily fluxes are in grey, while the black line shows the fluxes smoothed with a 40-day boxcar average). The multi-year mean daily total NH extratropical  $O_3$  STT flux is shown in red.

1

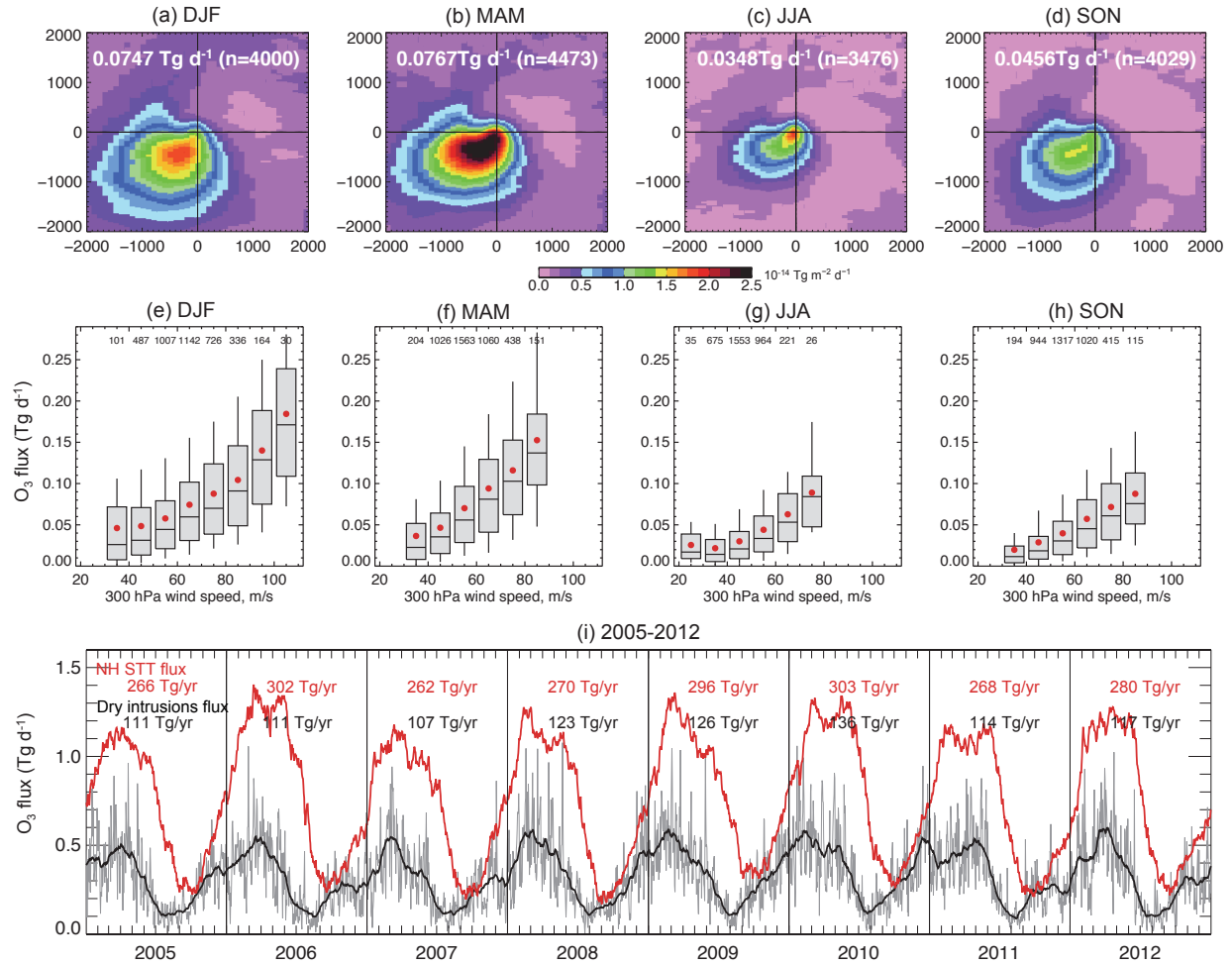


**Figure 11.** Daily, seasonal, and interannual variability in MERRA-2 STT O<sub>3</sub> fluxes for 2005-2012. Top row (a-d): Seasonal composites of O<sub>3</sub> STT fluxes (units of  $10^{-14}$  Tg O<sub>3</sub> m<sup>-2</sup> d<sup>-1</sup>). The mean daily composite fluxes and number of cyclones in each seasonal composite are indicated in the lower left of each panel. Middle row (e-h): dependence of dry intrusion STT O<sub>3</sub> flux on 300 hPa windspeed (maximum windspeed in southern quadrants of cyclone composite). The boxplots correspond to the 25<sup>th</sup> and 75<sup>th</sup> percentiles (grey box), 10<sup>th</sup> and 90<sup>th</sup> percentiles (whiskers), median (bar inside the grey box), and means (red filled circle) for each 10 m s<sup>-1</sup> bin. Bottom panel: Daily dry intrusion STT O<sub>3</sub> flux (grey line) for 2005-2012. The black line corresponds to the daily dry intrusion STT O<sub>3</sub> flux smoothed with a 40-day boxcar average. For comparison, the red line shows the daily MERRA-2 NH extratropical STT O<sub>3</sub> flux calculated with a mass conservation approach. For each year, the annual NH extratropical STT and dry intrusion O<sub>3</sub> fluxes are indicated.

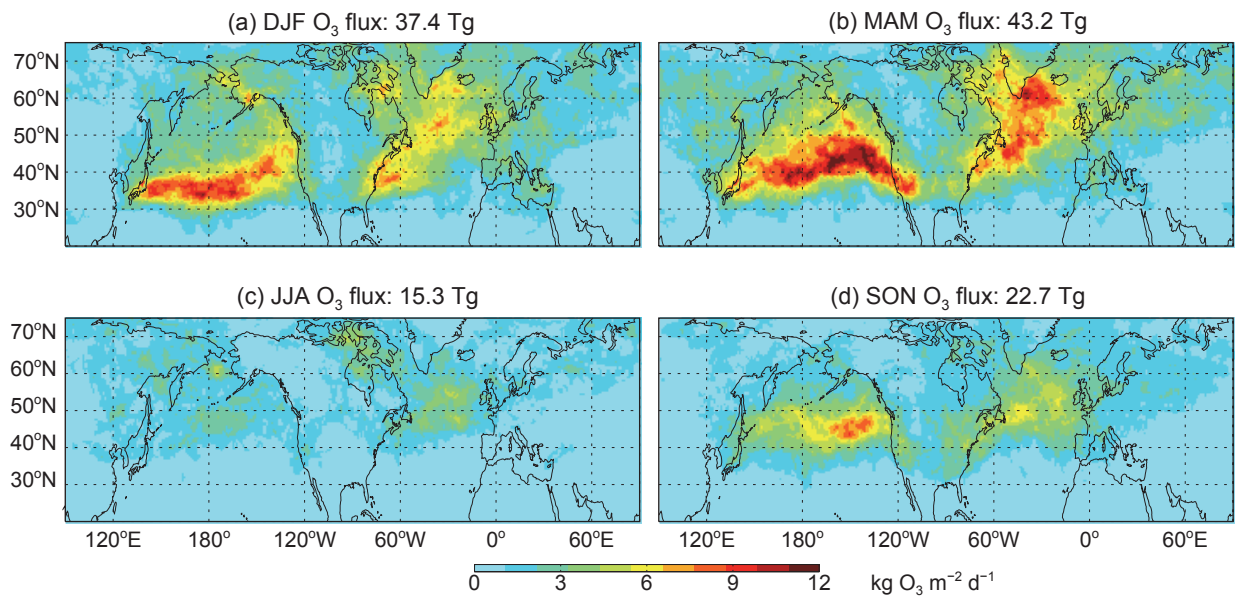


**Figure 12.** Spatial distribution of seasonally averaged O<sub>3</sub> STT flux ( $10^{-3}$  Tg O<sub>3</sub>) due to extratropical cyclones for 2005-2012.

**Multi-year composite view of ozone enhancements and stratosphere-to-troposphere transport in dry intrusions of northern hemisphere extratropical cyclones**

**Lyatt Jaeglé<sup>1</sup>, Robert Wood<sup>1</sup>, and Krzysztof Wargan<sup>2,3</sup>**

<sup>1</sup>Department of Atmospheric Sciences, University of Washington, Seattle, Washington, USA

<sup>2</sup>Science Systems and Applications Inc., Lanham, Maryland, USA

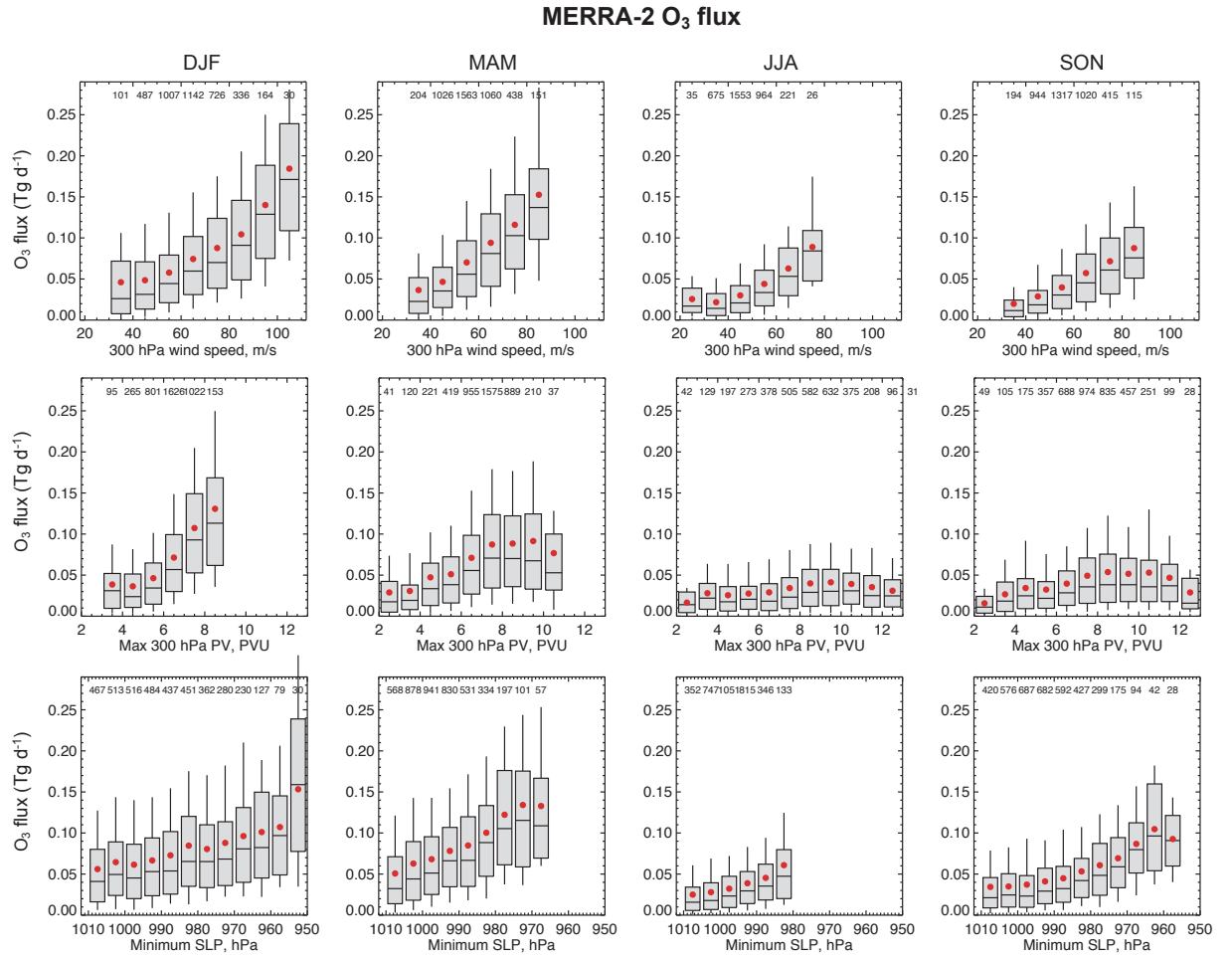
<sup>3</sup>Global Modeling and Assimilation Office, NASA Goddard Space Flight Center, Greenbelt, Maryland, USA

**Contents of this file**

Figures S1 to S4

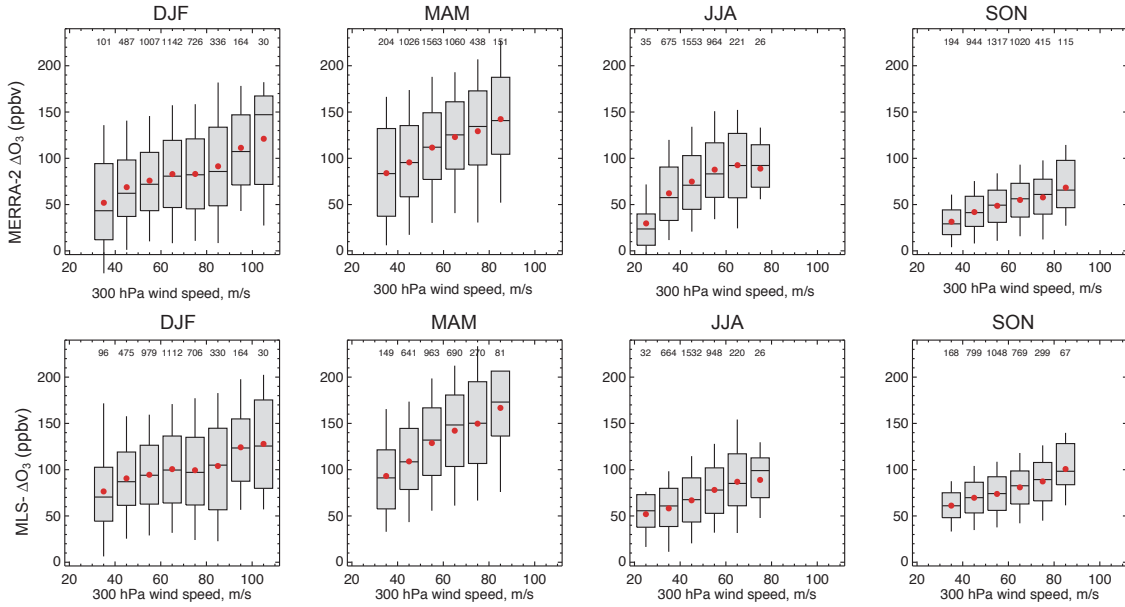
**Introduction**

Figure S1 shows the seasonal dependence of dry intrusion STT O<sub>3</sub> flux as a function of 300 hPa wind speed, 300 hPa PV, and minimum SLP. Figures S2 and S3 shows the seasonal dependence of dry intrusion  $\Delta\text{O}_3$  at 261 hPa and 464 hPa for MLS, TES, and MERRA-2. Figure S4 shows the sensitivity of our calculated dry intrusion STT O<sub>3</sub> flux to assumptions about different control surfaces.



**Figure S1.** Dependence of dry intrusion 2005-2012 MERRA-2 STT O<sub>3</sub> flux as a function of (top row) 300 hPa windspeed, (middle row) 300 hPa PV, and (bottom row) SLP. The boxplots correspond to the 25<sup>th</sup> and 75<sup>th</sup> percentiles (grey box), 10<sup>th</sup> and 90<sup>th</sup> percentiles (whiskers), median (bar inside the grey box), and means (red filled circle) for each bin.

### 261 hPa MLS and MERRA-2 $\Delta O_3$



**Figure S2.** Seasonal dependence of dry intrusion 261 hPa  $\Delta O_3$  for MERRA-2 (top row) and MLS (bottom row) as a function of 300 hPa windspeed. The boxplots correspond to the 25<sup>th</sup> and 75<sup>th</sup> percentiles (grey box), 10<sup>th</sup> and 90<sup>th</sup> percentiles (whiskers), median (bar inside the grey box), and means (red filled circle) for each bin. The  $\Delta O_3$  shown here are the same as in Figure 5b.

### 464 hPa TES and MERRA-2 $\Delta O_3$

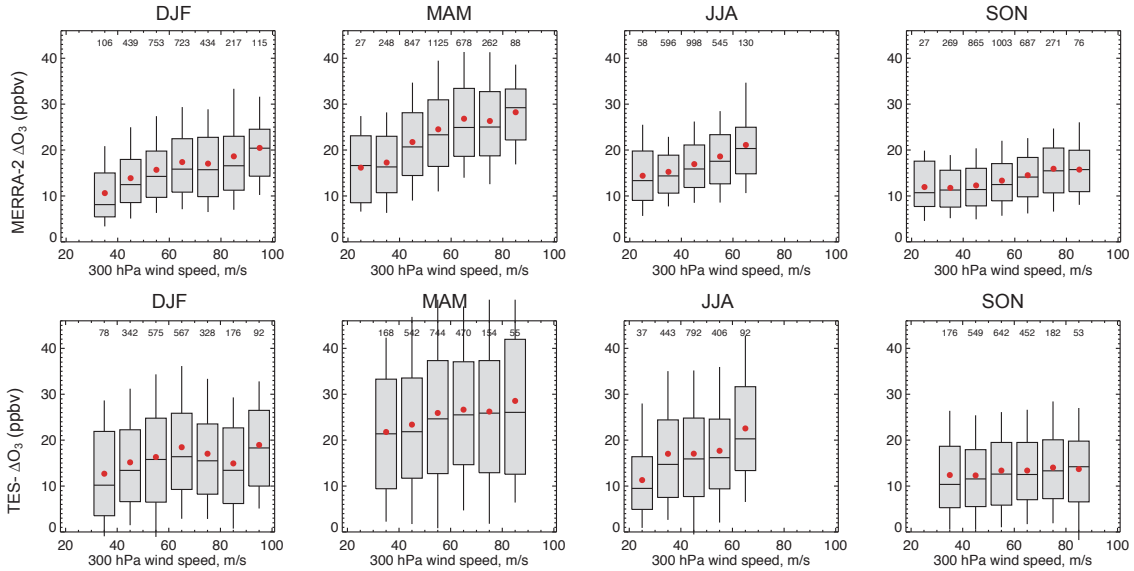


**Figure S3.** Seasonal dependence of dry intrusion 464 hPa  $\Delta O_3$  for MERRA-2 (top row) and TES (bottom row) as a function of 300 hPa windspeed. The boxplots correspond to the 25<sup>th</sup> and 75<sup>th</sup> percentiles (grey box), 10<sup>th</sup> and 90<sup>th</sup> percentiles (whiskers), median (bar inside the grey box), and means (red filled circle) for each bin. The  $\Delta O_3$  shown here are the same as in Figure 7b.

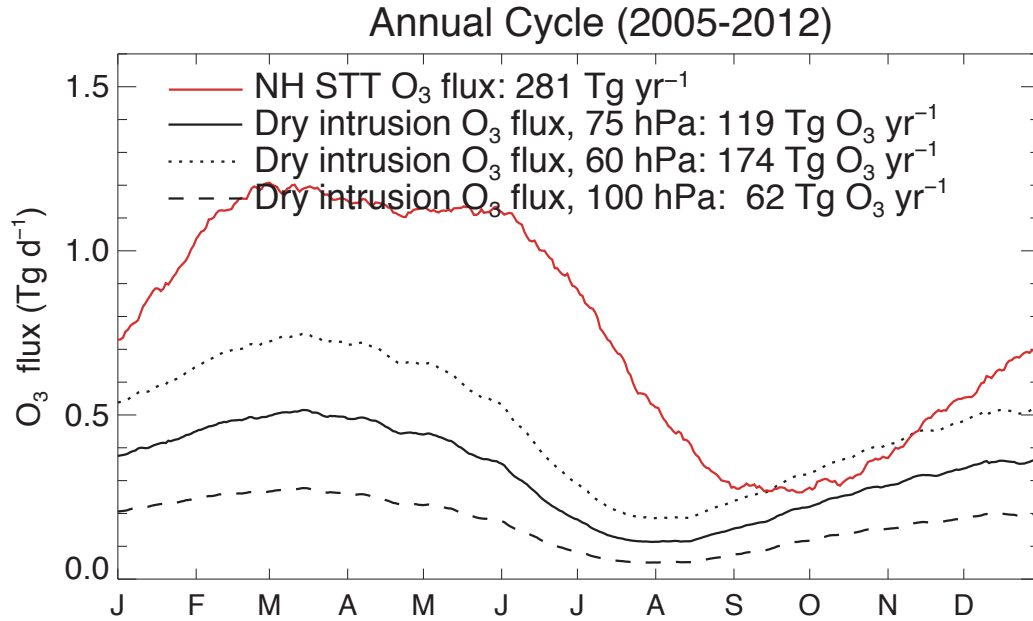


**Figure S4.** Annual cycle of dry intrusion stratosphere-to-troposphere transport (STT) of O<sub>3</sub> inferred from MERRA-2 for 2005-2012. The solid black line shows the DI STT flux if we assume that all the stratospheric O<sub>3</sub> between the local 2 pvu dynamical tropopause and the level 75 hPa below the climatological dynamical tropopause is irreversibly mixed. The dotted (dashed) black lines assume that O<sub>3</sub> between the local 2 pvu dynamical tropopause and the level 60 hPa (110 hPa) below the climatological dynamical tropopause is irreversibly mixed. The fluxes are smoothed with a 40-day boxcar average. The multi-year mean daily NH extratropical O<sub>3</sub> STT flux is shown in red.